Self-assembling dendrimer nanosystems for specific fluorine magnetic resonance imaging and effective theranostic treatment of tumors

Zhenbin Lyu, Brigino Ralahy, Teodora-Adriana Perles-Barbacaru, Ling Ding, Yifan Jiang, Baoping Lian, Tom Roussel, Xi Liu, Christina Galanakou, Erik Laurini, et al.

Self-assembling dendrimer nanosystems for specific fluorine magnetic resonance imaging and efficient theranostic treatment of tumors

Zhenbin LYU[1,2,#], Brigino RALAHY[1,#], Teodora-Adriana PERLES-BARBACARU[3,#], Ling DING[1,3,#], Yifan JIANG[1], Baoping LIAN[4], Tom ROUSSEL[1], Xi LIU[1,5], Christina GALANAKOU[1], Erik LAURINI[6], Aura TINTARU[2], Suzanne GIORGIO[1], Sabrina PRICL[6,7], Xiaoxuan LIU[4], Monique BERNARD[3], Juan IOVANNA[5], Angèle VIOLA[3], Ling PENG[1,*]

[1] Aix Marseille University, CNRS, Centre Interdisciplinaire de Nanoscience de Marseille (UMR 7325), Equipe Labellisée Ligue Contre le Cancer, 13288 Marseille, France

[2] Aix Marseille University, CNRS, Institut de Chimie Radicalaire (ICR), UMR 7273, 13013 Marseille, France

[3] Aix Marseille University, CNRS, Centre de Résonance Magnétique Biologique et Médicale (CRMBM), UMR 7339, 13385 Marseille, France

[4] State Key Laboratory of Natural Medicines and Jiangsu Key Laboratory of Drug Discovery for Metabolic Diseases, Center of Drug Discovery, Center of Advanced Pharmaceuticals and Biomaterials, China Pharmaceutical University, 431007 Nanjing, P. R. China

[5] Centre de Recherche en Cancérologie de Marseille, INSERM U1068, CNRS, UMR 7258, Institut Paoli-Calmettes, Aix Marseille Université, 13273 Marseille, France

[6] Molecular Biology and Nanotechnology Laboratory (MolBNL@UniTS), DEA, University of Trieste, 34127 Trieste, Italy

[7] Department of General Biophysics, Faculty of Biology and Environmental Protection, University of Lodz, 90-236 Lodz, Poland

[#] These authors contributed equally

[*] ling.peng@univ-amu.fr

Abstract (<250 words)

Fluorine magnetic resonance imaging (^{19}F-MRI) is particularly promising for biomedical applications owing to the absence of fluorine in most biological systems. However, its use has been limited by the lack of safe and water-soluble imaging agents with high fluorine contents and suitable relaxation properties. We report innovative ^{19}F-MRI agents based on supramolecular dendrimers self-assembled by an amphiphilic dendrimer composed of a hydrophobic alkyl chain and a hydrophilic dendron. Specifically, this amphiphilic dendrimer bears multiple negatively charged terminals with high fluorine content, which effectively prevented intra- and intermolecular aggregation of fluorinated entities via electrostatic repulsion. This permitted high fluorine nuclei mobility alongside good water solubility with favorable relaxation properties for use in ^{19}F-MRI. Importantly, the self-assembling ^{19}F-MRI agent was able to encapsulate the near-infrared fluorescence (NIRF) agent DiR and the anticancer drug paclitaxel for multimodal ^{19}F-MRI and NIRF imaging of and theranostics for pancreatic cancer, a deadly disease for which there remains no adequate early detection method or efficacious treatment. The ^{19}F-MRI and multimodal ^{19}F-MRI and NIRF imaging studies on human pancreatic cancer xenografts in mice confirmed the capability of both imaging modalities to specifically image the tumors and demonstrated the efficacy of the theranostic agent in cancer treatment, largely outperforming the clinical anticancer drug paclitaxel. Consequently, these dendrimer nanosystems constitute promising ^{19}F-MRI agents for effective cancer management. This study offers a new avenue to explore for the construction of ^{19}F-MRI agents and theranostics, exploiting self-assembling supramolecular dendrimer chemistry.

Keywords:

dendrimer, self-assembly, magnetic resonance imaging, cancer detection, cancer treatment,

Significance statement (< 120 words)

Bioimaging plays an important role in diagnosing and treating disease. We constructed innovative agents for fluorine magnetic resonance imaging (^{19}F-MRI), an emerging imaging modality to complement the widely used ^{1}H-MRI by adding specificity. These ^{19}F-MRI agents are based on an amphiphilic dendrimer bearing negatively charged fluorinated terminals, enabling high fluorine contents yet without fluorine-fluorine aggregation, leading to excellent relaxation characteristics and good water solubility for use in ^{19}F-MRI. Importantly, this self-assembling ^{19}F-MRI agent could also encapsulate fluorescence dye and anticancer drug enabling ^{19}F-MRI-based multimodal imaging and theranostics in cancer detection and treatment. This study demonstrates the strong potential for modular self-assembling dendrimers in the construction of imaging and theranostic agents for biomedical applications.

Introduction

Proton magnetic resonance imaging (^{1}H-MRI) is one of the most widely used biomedical imaging techniques.[1-2] It provides anatomic, functional and metabolic information at high spatial resolution yet with unlimited tissue penetration. In clinical ^{1}H-MRI, contrast agents can be administered to enhance the image contrast in a number of applications.[3] However, identifying differences in contrast between diseased tissues and surrounding tissues can remain challenging in ^{1}H-MRI, as H_2O constitutes over 70% of the body weight. Interest in using fluorine magnetic resonance imaging (^{19}F-MRI) with fluorinated imaging agents is increasing[4-6] because fluorine is absent in most biological systems, and using exogenous ^{19}F-MRI agents provides background-free images with high specificity that complement with ^{1}H-MRI.

Current ^{19}F-MRI is limited to detecting ^{19}F-MRI signals when the fluorine concentration is low. ^{19}F-MRI agents with high contents of chemically equivalent fluorine nuclei need to be employed to generate sharp and intense ^{19}F-MRI signals to overcome this limitation.[4-6] However, compounds with high fluorine contents are both hydrophobic and lipophobic, so they tend to be heavily aggregated and poorly soluble in water, hampering the mobility of ^{19}F nuclei hence attenuating the ^{19}F-MRI signal.[6-8] The fluorine nuclei mobility and content as well as water solubility of a ^{19}F-MRI agent therefore need to be delicately balanced. Various ^{19}F-MRI agents have been explored,[4-6] including perfluorocarbon nanoemulsions,[9-11] agents with hyperbranched or dendritic architecture,[12-19] and functional fluorinated groups.[20-23] However, all such agents had limitations such as low signal-to-noise ratio (SNR), low fluorine content, instability or insolubility in water.

We have recently developed modular and adaptive self-assembling dendrimer nanosystems composed of amphiphilic dendrimers for the sensitive and specific detection of cancer.[24-27] These nanosystems exploit the cooperative multivalency of dendrimers alongside passive tumor targeting via the enhanced permeability and retention (EPR) effect[28-31] for effective tumor detection. Amphiphilic dendrimers combine the self-assembling abilities of amphiphiles with dendritic structures, hence readily form nanomicellar systems.[32-34] The high structural symmetry and multivalency of the dendritic scaffold make them ideal platforms for constructing ^{19}F-MRI agents. Indeed, fluorinated moieties can be introduced at the terminals to achieve the required high content of chemically equivalent fluorine nuclei for sharp ^{19}F-MRI signals (Fig. 1). In addition, the supramolecular dendrimer nanomicelles can be loaded with hydrophobic imaging agents and drug candidates to allow ^{19}F-MRI-based multimodal imaging and theranostics (Fig. 1A).

In this study, we designed and synthesized amphiphilic dendrimers **1a**, **1b** and **1c** with negatively charged fluorinated entities at the dendrimer terminals (Fig. 1B) for use as innovative agents for ^{19}F-MRI. These amphiphilic dendrimers harbor evenly distributed CF_3 moieties with adjacent carboxylate groups at the terminals. The negatively charged carboxylate terminals not only increase the water solubility, but also generate strong charge–charge repulsion, preventing the CF_3 groups from aggregation and hence maintaining fluorine nuclei mobility for generating strong ^{19}F-MRI signals. Specifically, **1c** is non-toxic and self-assembled into supramolecular dendrimer nanomicelles with favorable properties for use in ^{19}F-MRI. The hydrophobic core of the supramolecular dendrimer formed by **1c** were further loaded with the near-infrared fluorescent (NIRF) dye DiR and the anticancer drug paclitaxel (PTX). Encapsulation of these hydrophobic agents inside the supramolecular dendrimer core had negligible impact on the relaxation properties of ^{19}F nuclei on the surface because the core was segregated in space from the surface. This enabled

effective multimodal ^{19}F-MRI and NIRF imaging and ^{19}F-MRI-based theranostics for simultaneous detection and treatment of cancer. These results highlight the potential of self-assembling supramolecular dendrimers in the construction of imaging agents for biomedical ^{19}F-MRI applications.

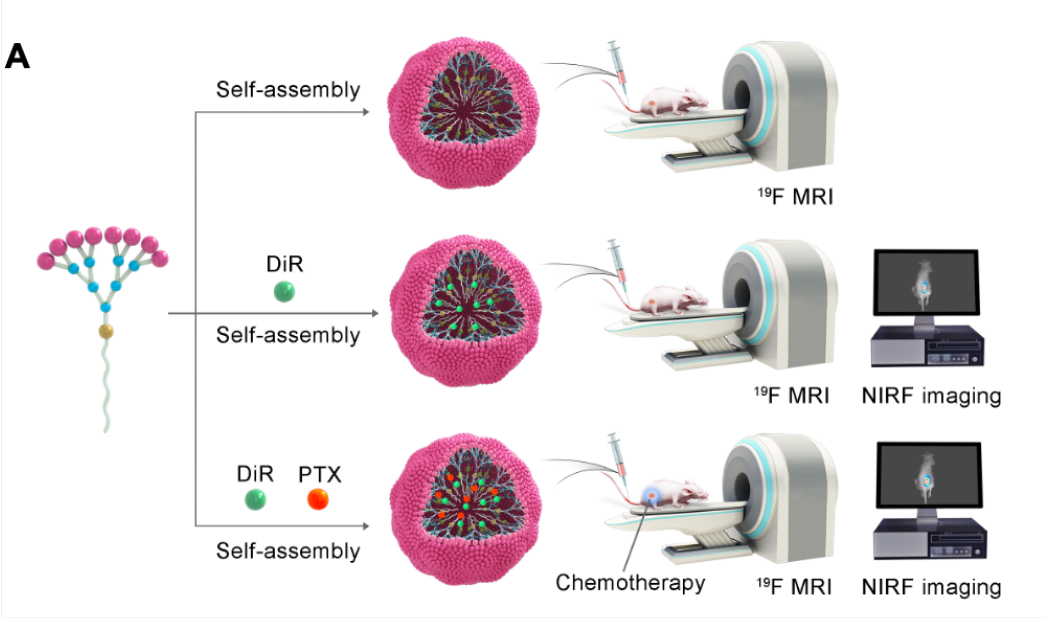

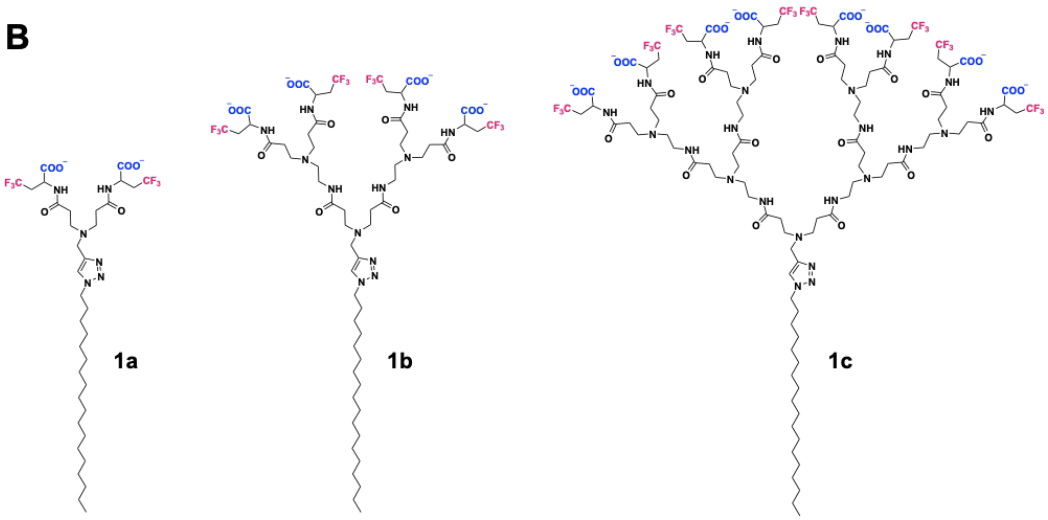

Fig. 1 Schematic illustration of self-assembling supramolecular dendrimer nanosystems for fluorine magnetic resonance imaging (^{19}F-MRI), ^{19}F-MRI-based multimodal imaging and theranostics. (A) Self-assembly of a fluorinated amphiphilic dendrimer into nanomicelles in the absence and/or presence of the NIRF probe DiR and the anticancer drug paclitaxel (PTX) within the supramolecular dendrimer core for ^{19}F-MRI, bimodal ^{19}F-MRI and NIRF imaging as well as ^{19}F-MRI-based theranostics for cancer detection and treatment. (B) Chemical structures of the amphiphilic dendrimers **1a–c** designed and studied for ^{19}F-MRI.

Results and discussion

Robust and reliable synthesis of fluorinated dendrimers

We first synthesized the fluorinated amphiphilic dendrimers **1a**, **1b**, and **1c** starting with the ester-terminated dendrimers **2a**, **2b** and **2c**, respectively (Fig. 2A). **2a–c** were prepared using previously published methods,[35] and were then hydrolyzed[36] to give the carboxylic-acid-terminating dendrimers **3a–c**. Coupling **3a–c** with the fluorinated building block **F-Ala** (a fluorinated derivative of alanine) gave **4a–c**, which were then hydrolyzed to give the target dendrimers **1a–c** (Figs. 2A and S1). This robust synthesis readily gave gram-scale quantities of **1c**.

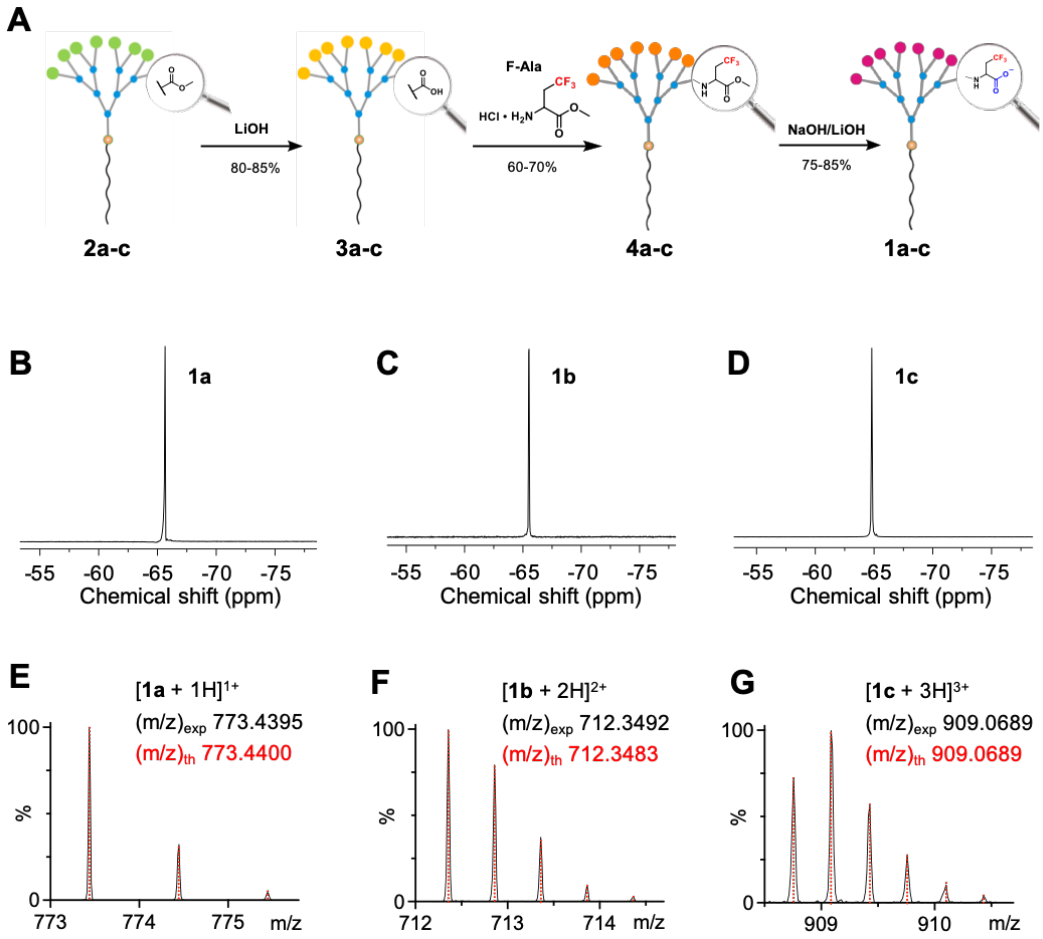

Fig. 2 Synthesis and characterization of the fluorinated amphiphilic dendrimers **1a–c**. (A) Synthesis scheme for **1a**, **1b**, and **1c** starting with ester-terminating dendrimers **2a**, **2b**, and **2c**, respectively. (B, C, and D) fluorine nuclear magnetic resonance (^{19}F-NMR) spectra and (E, F, and G) molecular peaks in high-resolution mass spectroscopy (HRMS) of **1a**, **1b**, and **1c**.

The synthesized **1a-c** were examined and characterized using ^{1}H-, ^{19}F-, ^{13}C-nuclear magnetic resonance (NMR) analysis, and high-resolution mass spectroscopy (HRMS) for their structural integrity and compositional purity (Fig. 2B–2G and Fig. S2). As expected, **1a–c** gave sharp and intense characteristic singlet ^{19}F-NMR peaks (Fig. 2B–2D). Specifically, **1c** contains 24 chemically equivalent fluorine nuclei and has a fluorine content of 16.7% by weight, which is higher than that

of many ^{19}F-MRI agents reported in the literature.[4-6] Remarkably, the high fluorine content did not compromise the solubility of **1c**, which readily dissolved in water to give a clear solution, even at a concentration of 85 mg/mL. The exceptional solubility of **1c** can be mainly ascribed to the presence of negatively charged carboxylate terminals, which significantly enhance the water solubility of **1c** while preventing aggregation of the fluorinated entities via electrostatic repulsion.

Dendrimer 1c is non-toxic despite having a high fluorine content

Prior to any biomedical study, the safety profile of the employed agent needs assessing, particularly ^{19}F-MRI agents due to the high concentrations that are often required. We therefore first assessed the cytotoxicity of **1a–c** on various cell lines (human kidney cells HEK293, murine fibroblast cells L929, and murine ovarian cells CHO-K1) using the PrestoBlue test and the lactate dehydrogenase (LDH) assay. The PrestoBlue test measures cell viability associated with cellular metabolic activity, whereas the LDH assay evaluates cell death related to membrane damage as measured by LDH release. At concentrations up to 1.0 mM, **1c** showed no metabolic toxicity or membrane damage in any of the tested cells (Fig. 3A and 3B), in contrast to **1a** which was highly toxic at concentrations above 0.25 mM and **1b** showing marked toxicity in HEK293 at a concentration of 0.50 mM (Fig. 3A). This discrepancy in toxicity may be due to the stronger hydrophobicity of the lower generation dendrimers leading to a higher affinity towards the cell membranes. The cell membranes would thereby destabilize more readily with the lower generation dendrimers, hence their higher cytotoxicity compared to the higher generation dendrimers.

The cytotoxicity of **1a** and **1b** led to us focusing our further studies only on **1c**. We then assessed the hemolytic toxicity of **1c**. The hemolysis assay using mouse red blood cells revealed that **1c** had very low hemolytic activity (~10%), even at 1.0 mM (Fig. S3A). This result is in line with those obtained using LDH assay, as might be expected since both hemolysis and LDH assays measure cytotoxicity related to cell membrane integrity upon treatment with **1c**.

We next assessed the toxicity of **1c** i*n vivo* by evaluating the inflammatory response and blood biochemistry, as well as histological analysis of major organs in healthy mice (Fig. 3C-3E). Our results show that **1c** induced no significant inflammatory response: the levels of the inflammatory factors IL-1β, IL-6, TNF-α, and INF-γ were similar to those found in the negative control group of mice treated with PBS buffer (Figure 3C); mice in the positive control group treated with lipopolysaccharide (LPS) on the other hand showed significantly increased levels of IL-1β, IL-6, TNF-α, and INF-γ (Figure 3C).

Major blood biochemical markers (alanine transaminase (ALT), aspartate transaminase (AST), urea, creatinine (CREA), triacylglycerol (TG), and total cholesterol (TCHO)) remained normal (Fig. 3D) following **1c** administration, indicating normal functioning of the major organs (including the liver and kidneys) and underlining good biocompatibility of **1c**. Histological analysis of the major organs revealed no pathological changes either (Fig. 3E). The lack of cytotoxic effects, inflammatory responses and signs of pathology in major organs highlights the good safety profile for **1c**.

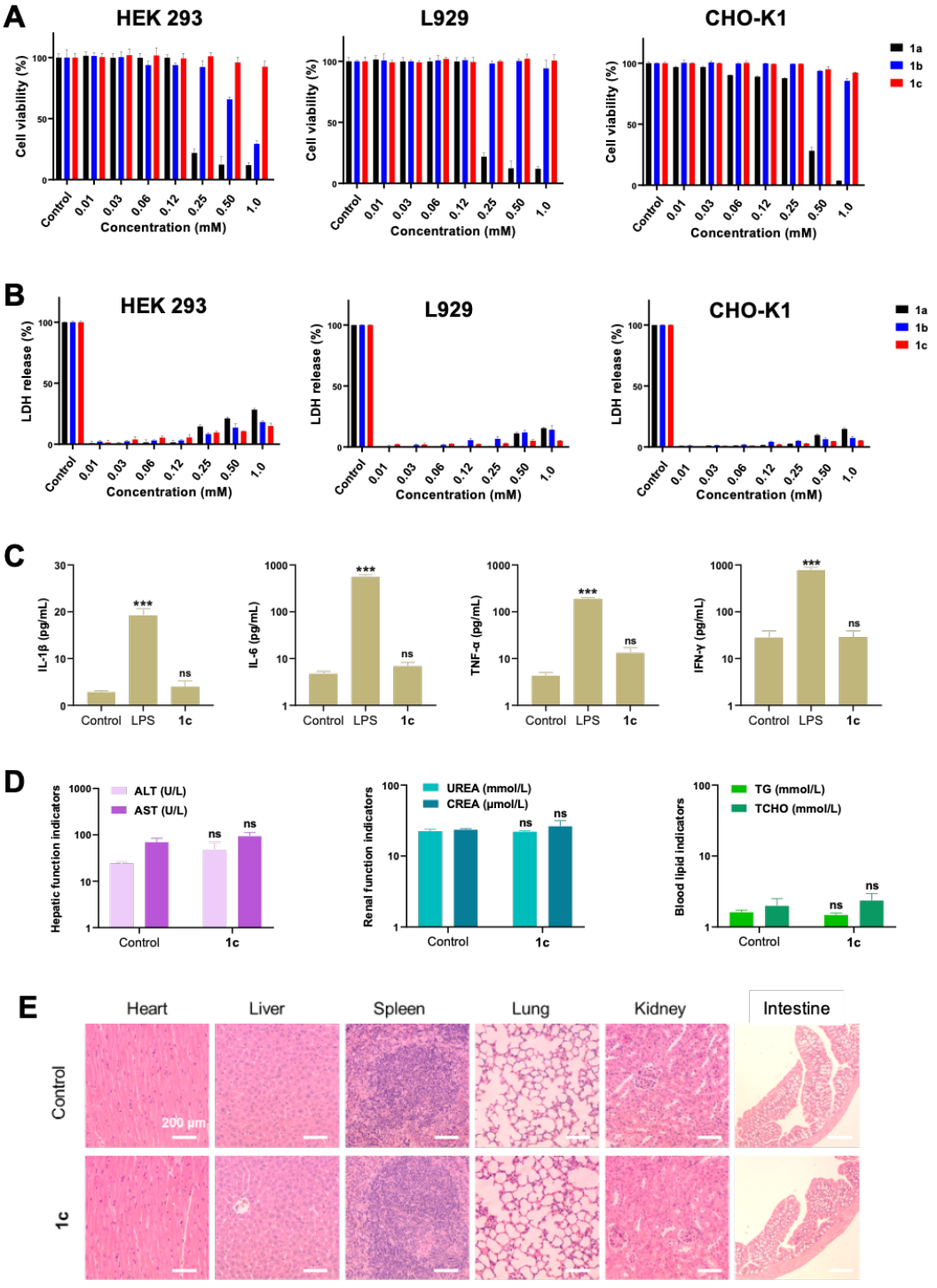

Fig. 3 Toxicity and safety evaluation of **1a–c**. (A) Cytotoxicity evaluation of **1a–c** on human kidney cells HEK293, murine fibroblast cells L929, and murine ovarian cells CHO-K1 using PrestoBlue assay. A non-treatment was used as the control. (B) Evaluation of membrane damage by **1a–c** on HEK293, L929, CHO-K1 using lactate dehydrogenase (LDH) release assay. A non-treatment was used as a negative control, and lysis buffer was used as a positive control for the LDH assay. Each result represents the mean ± standard deviation (n=3). (C, D, and E) *In vivo* safety evaluation results for healthy mice treated with **1c**. Mice were intravenously administered **1c** (286.5 mg/kg) or PBS (control) or intraperitoneally administered lipopolysaccharide (LPS) (5.0 mg/kg) as a positive

control. (C) Concentrations of the inflammatory cytokines IL-1β, IL-6, TNF-α and INF-γ in the mouse serum samples. (D) Liver and kidney function results. Alanine transaminase (ALT), aspartate transaminase (AST), urea, creatinine (CREA), triglyceride (TG), and total cholesterol (TCHO) concentrations in mouse serum. Each result represents the mean ± standard deviation (n=3). Statistical significance was calculated using two-tailed Student's t-test and one-way ANOVA with Tukey's multiple comparison test. (ns = not significant, *** = p≤0.001, *vs* PBS control). (E) Histology of the main organs using hematoxylin and eosin staining (scale bar = 200 μm).

Self-assembly of 1c into nanomicelles with favorable relaxation properties for ^{19}F-MRI

The amphiphilicity enabled **1c** to spontaneously self-assemble into nanoparticles (referred as to **1c**@ hereafter) in water, as confirmed by dynamic light scattering (DLS) analysis (Fig. 4A). The transmission electron microscopy (TEM) image of **1c**@ (Fig. 4B) confirmed the presence of small, uniform, spherical particles measuring ~25 nm in size consistent with the typical characteristics of nanomicelles. Further fluorescence spectroscopic analysis revealed a critical micelle concentration (CMC) of ~120 μM (Fig. 4C). The self-assembling process of the amphiphilic dendrimer **1c** into the nanoparticle **1c**@ was also investigated using a rigorously validated methodology rooted in isothermal titration calorimetry (ITC) technique.[37-38] The ITC experiments (Fig. 4D/E) yielded a CMC of 153 μM, a value consistent with the data obtained using fluorescence spectroscopy. Thermodynamic analysis of the demicellization process indicated predominantly exothermic signals upon injection of concentrated **1c** solution into water, while the reverse micellization process exhibited a corresponding positive (endothermic) micellization enthalpy value (ΔH_{mic} = +1.46 ± 0.16 kcal/mol), deduced from the integrated demicellization data fit as the difference between final and initial heat in the titration curve (Fig. 4E). Moreover, the use of the ITC protocol enabled the determination of the aggregation number (N_{agg}) for **1c**@ as 48 ± 2.

To substantiate the spontaneous aggregation of **1c** into **1c**@, extensive atomistic molecular dynamics (AMD) simulations spanning 500 nanoseconds were conducted. Starting from a randomized distribution of 48 molecules of **1c** in solution, the AMD simulations yielded a stable **1c**@ nanoassembly, as visually depicted in Fig. 4F. The resulting average micelle gyration radius (R_g**1c**@) was calculated as 9.0 ± 0.2 nm (Fig. 4G), consistent with the dimensional assessments obtained using DLS and TEM methodologies. Furthermore, a detailed examination of the conformational characteristics of the formed **1c**@ nano-assemblies, along with the radial distribution analysis of the CF_3 terminal groups, unveiled the absence of backfolding and the optimal positioning of all CF_3 moieties at the micellar periphery (Fig. 4G).

Indeed, the ^{19}F-NMR peak of **1c**@ remained remarkably sharp and intense even at 3.0 mM **1c** (>>CMC) in an aqueous solution (Fig. 4H), with the peak line width (full-width at half-maximum, FWHM) of 23 Hz, similar to that obtained in organic solvent (38Hz) (Fig. 2D). This finding indicated the chemical equivalence and high mobility of all the fluorine nuclei in **1c**@, thus confirming fulfillment of our design concept and aim for ^{19}F-MRI.

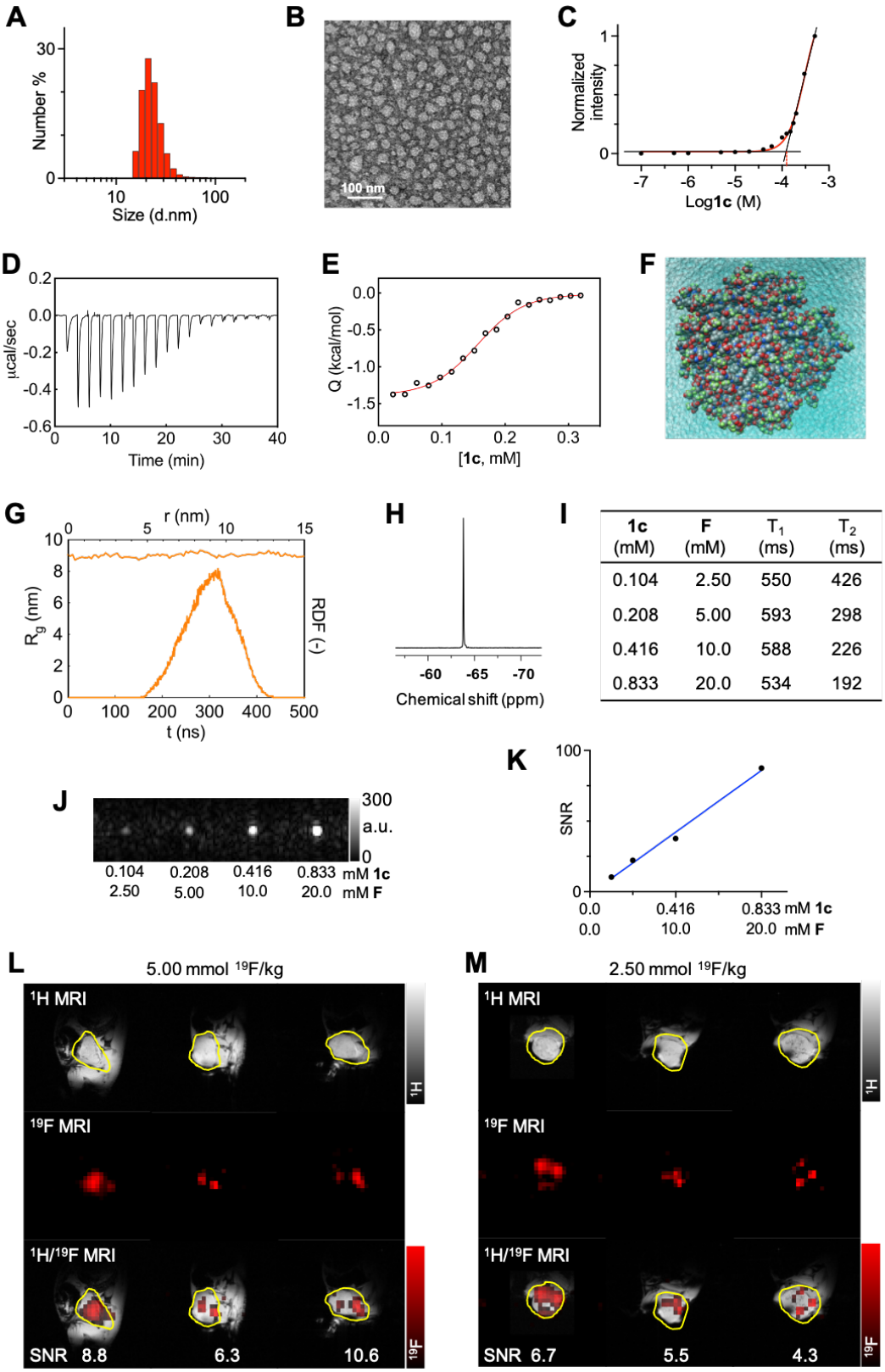

Fig. 4 Self-assembling of the amphiphilic dendrimer **1c** into nanomicelles **1c**@ for use as an imaging agent for fluorine magnetic resonance imaging (^{19}F-MRI). (A) Dynamic light scattering results and (B) transmission electron microscopy image of the self-assembled **1c**@ nanomicelles. (C) Critical micellar concentration (CMC) of **1c** estimated using a fluorescence spectroscopic assay with Nile

Red. (D) ITC raw thermogram as obtained for the **1c**@ demicellization process. (E) Representative ITC profiles for the demicellization process of **1c**@ in water. The solid red line is a data fitting with a sigmoidal function. (F) Zoomed snapshot from the equilibrated AMD trajectory of **1c**@ (C, gray; N, blue; O, red; F, light green). Water molecules are shown as transparent aqua spheres, while all hydrogen atoms have been omitted for clarity. (G) Average radius of gyration (R_g) of **1c**@ as a function of time t (left y axis, blue curve) and radial distribution function (RDF) of the CF_3 terminals as a function of the distance r from the center of mass of **1c**@ (right y axis, green curve) during the equilibrated AMD trajectory. (H) ^{19}F-nuclear magnetic resonance spectrum of **1c**@ (3.0 mM **1c** in D_2O) recorded with a 400MHz NMR spectrometer (376 MHz for ^{19}F) at 25°C. (I) ^{19}F magnetic resonance relaxation time constants (T_1 and T_2) for **1c**@ at a magnetic field strength of 7 T and 20°C. (K) *In vitro* ^{19}F-MR images and (K) ^{19}F-MRI signal-to-noise ratio (SNR) of **1c**@ at four different concentrations of **1c** and fluorine. (L, M) *In vivo* ^{1}H-MR anatomical images (top), ^{19}F-MR images (middle), and overlay of ^{1}H-MR and ^{19}F-MR images (bottom) of tumors in L-IPC xenograft mice 24 h after intravenous injection of **1c**@ at **1c** concentrations of (L) 0.208 mmol/kg and (M) 0.104 mmol/kg (corresponding to fluorine concentrations of 5.00 and 2.50 mmol/kg, respectively). MR images were acquired in the sagittal plane with respect to the mouse.

Further evaluation of **1c**@ using an MRI scanner at 7T revealed favorable T_1 and T_2 relaxation time constants (Fig. 4I). A short spin–lattice relaxation time constant (T_1) allows a short ^{19}F-MRI acquisition time, whereas a long spin–spin relaxation time constant (T_2) prevents rapid signal decay, meaning the ^{19}F-MRI signal can be readily acquired with MRI sequences using conventional readout trajectories.[4] The T_1 values for **1c**@ at fluorine concentrations of 2.50–20.0 mM were in the range of 534–593 ms, which were comparable to T_1 values for the most often used ^{19}F-MRI agents.[4-6] Remarkably, the T_2 values for **1c**@ at various concentrations were in the range of 192–426 ms, which are all above 190 ms and much higher than the T_2 values for the most commonly used ^{19}F-MRI agents.[4-6] The high T_2 values confirmed the high mobility of the fluorine nuclei in **1c**@ supported by our design concept using charged terminals to create strong electrostatic repulsion, thereby preventing aggregation of neighboring fluorinated moieties.

The excellent T_2 relaxation time constants of **1c**@ prompted us to perform phantom studies to assess the ^{19}F-MRI performance (Fig. 4J). We detected a weak but measurable signal even at 0.104 mM **1c** (2.50 mM fluorine) with an acquisition time of 30 min, considered acceptable for in vivo imaging in clinical settings. Importantly, the ^{19}F-MRI signal intensity was directly proportional to **1c** concentration (Fig. 4K), facilitating quantitative analysis.

The promising ^{19}F-MRI properties and safety profile of **1c**@ encouraged us to perform *in vivo* ^{19}F-MRI of cancer as a proof-of-concept study. We chose as our model the most deadly form of cancer - pancreatic cancer - for which there is still no efficacious treatment or early diagnosis imaging modality.[39-41] The most effective treatment remains surgical ablation, however, the tumor boundaries for small lesions or metastases (tumor diameter <2.0 cm) are currently difficult to determine by ^{1}H-MRI.[41] The development of novel non-invasive imaging modalities that allow specific tumor detection would help overcome this obstacle and is of paramount importance for pancreatic cancer.

In this study, we used a patient pancreatic tumor-derived xenograft mouse model L-IPC,[24, 42] and administered **1c** intravenously at doses of 0.208 and 0.104 mmol/kg, corresponding to fluorine doses

of 5.00 and 2.50 mmol/kg, respectively. Both dendrimer doses gave ^{19}F-MRI signals that co-localized with the tumors on ^{1}H-MRI (Fig. 4L and 4M). We detected no ^{19}F-MRI signals in tissues surrounding the tumor, confirming the tumor-specific localization permitted by ^{19}F-MRI with **1c**@. This specificity for tumor detection can be ascribed to the unique dendritic multivalency of **1c**@ and the nanosize allowing effective accumulation within the tumor lesions via the EPR effect. This phenomenon, caused by leaky vasculature and dysfunctional lymphatic drainage within the tumor microenvironment, permitted an increased accumulation and local concentration of **1c** in disease lesion and thereby effective imaging and detection of the tumor. Noteworthy is the heterogenous distribution of ^{19}F-MRI hot-spot signals within the tumor tissue, which can be attributed to the particular heterogeneity of pancreatic cancer tumors with rich stroma and a heterogenous vascular supply.[43]

It should be mentioned that no mice treated with **1c**@ exhibited any abnormal behavior or signs of major organ pathology (Fig. S3B). These results corroborated well with those following administration of **1c**@ to healthy mice (Fig. 3E).

^{19}F-MRI-based multimodal imaging

Incorporating multiple imaging modalities into one nanosystem offers the advantage of providing complementary imaging information favoring a more sensitive and accurate diagnosis. Combining MRI, possessing high resolution with no penetration limitation, with fluorescence imaging[44-45] offering high sensitivity but limited penetration depth, would provide powerful bimodality imaging for cancer detection. We therefore encapsulated the near-infrared fluorescent dye DiR within the supramolecular dendrimer formed by **1c** for bimodal ^{19}F-MRI and NIRF imaging. Using the film dispersion method,[27] the resulting nanoparticles DiR/**1c**@ were small (Fig. 5A), having size around 31 nm, which is comparable to **1c**@ (Fig. 4B). This can be ascribed to the effective encapsulation of DiR within the supramolecular dendrimer core.

DiR/**1c**@ retained the characteristic fluorescence of DiR (Fig. 5B) as shown with free DiR in an organic solvent (Fig. S4). DiR/**1c**@ also showed similar relaxation time constants (Fig. 5C, Tab. S2) and ^{19}F-MRI properties to **1c**@ (Fig. 5D). Similar to with **1c**@ **(**Fig. 4F/G), the ^{19}F-MRI signal intensity increased linearly as the fluorine concentration increased **(**Fig. 5D/E). These results indicate that DiR/**1c**@ neither altered the NIRF properties of DiR nor the ^{19}F-MRI properties of **1c**. This can be ascribed to the fact that DiR is encapsulated within the hydrophobic inner core, whereas the fluorinated groups are on the hydrophilic outer surface of DiR/**1c**@. The two imaging modalities are thus sufficiently segregated in space to prevent their interference. The retained fluorine mobility and relaxation properties of **1c**@ with fluorescence properties of DiR hence accomplished the prerequisites for DiR/**1c**@ to be used for multimodal ^{19}F-MRI and NIRF imaging.

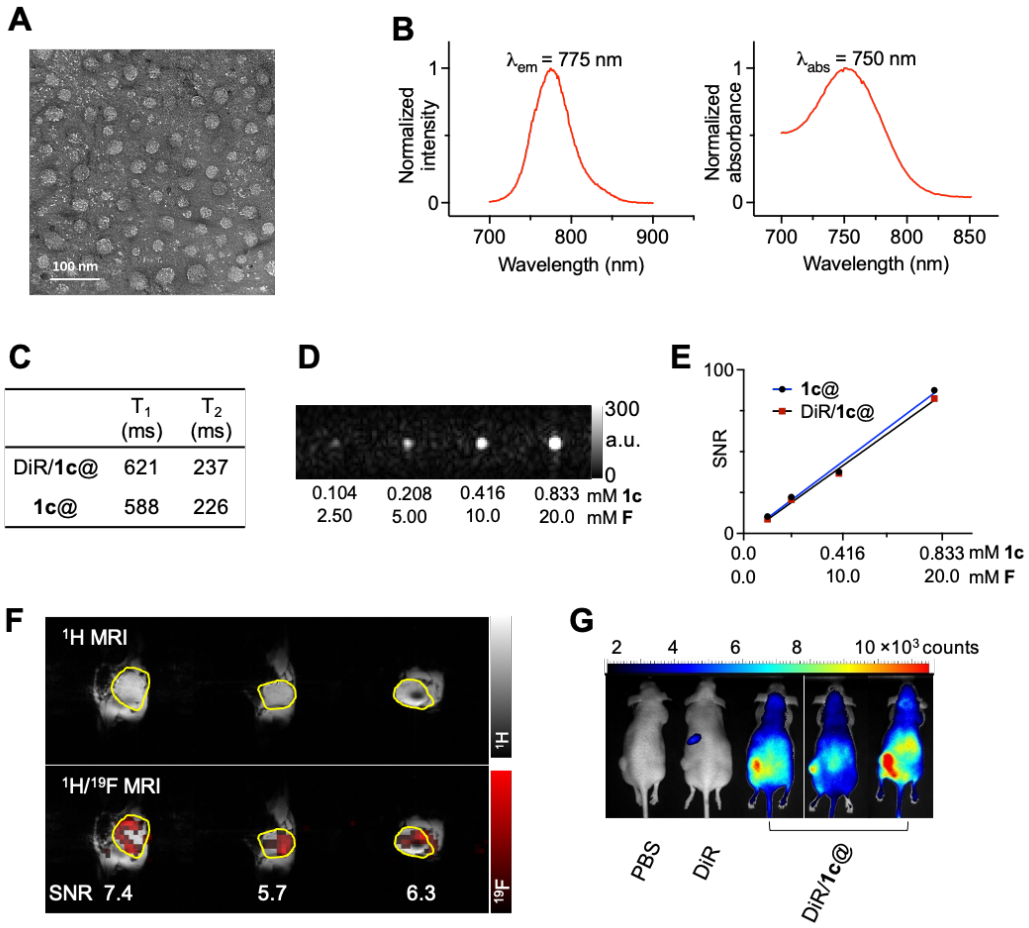

Fig. 5 Nanoprobe DiR/**1c**@ for detecting tumors using multimodal fluorine magnetic resonance imaging (^{19}F-MRI) and near-infrared fluorescence (NIRF) imaging. (A) Transmission electron microscopy (TEM) image of DiR/**1c**@. (B) Normalized absorbance (right) and fluorescence emission (left) spectra of DiR/**1c**@. (C) ^{19}F magnetic resonance relaxation time constants (T_1 and T_2) for DiR/**1c**@ compared to **1c**@ at a magnetic field strength of 7 T, 20°C and 10 mM fluorine. (D) ^{19}F-MRI of DiR/**1c**@ at different concentrations of **1c** and fluorine. (E) ^{19}F-MRI signal-to-noise ratio (SNR) at 7T for **1c**@ and DiR/**1c**@ at various concentrations of **1c** and fluorine. (F) *In vivo* ^{1}H-MRI (top) and ^{19}F-MRI superimposed on ^{1}H-MRI (bottom) of tumors in three different L-IPC xenograft mice 24 h after intravenous injection of DiR/**1c**@. (G) Fluorescence images in L-IPC xenograft mice 24 h after intravenous injection of PBS, DiR and DiR/**1c**@ (DiR: 80 μg/kg, F: 5.00 mmol/kg). MR images were acquired in the sagittal plane with respect to the mouse.

We therefore tested the in vivo performance of DiR/**1c**@ for multimodality MRI and NIRF imaging. ^{19}F-MRI hot-spot signals detectable in L-IPC xenograft mice treated with DiR/**1c**@ co-localized with tumors on anatomical ^{1}H-MR images (Fig. 5F). These results support the effective tumor imaging achieved using ^{19}F-MRI with DiR/**1c**@. We then performed NIRF imaging on the same mice having undergone ^{19}F-MRI. Tumor sites in mice treated with DiR/**1c**@ showed strong and intense fluorescence signals, in line with the ^{19}F-MRI results, whereas control mice treated with either PBS or DiR showed no detectable fluorescence signals (Fig. 5G). These results demonstrate the effectiveness of DiR/**1c**@ as a multimodal ^{19}F-MRI and NIRF imaging agent for tumor detection.

^{19}F-MRI-based theranostics for treating cancer

Theranostics, integrating therapeutic and diagnostic capacities in the same nanosystem, offers great promise for precision cancer treatment.[46-47] It promotes personalized medicine by enabling the individual monitoring of treatment effect and response in real time to ensure therapeutic efficacy. We investigated the potential use of **1c** in theranostics by encapsulating the anticancer drug paclitaxel (PTX) within the supramolecular dendrimer core using film dispersion method.[48-49] We also encapsulated the near-infrared fluorescence dye DiR within the PTX/**1c**@ to enable the detection of tumors using multimodal MRI and NIRF imaging. The so-obtained PTX/DiR/**1c**@ showed high drug loading (23%) and produced a sharp and intense singlet ^{19}F-NMR signal (Fig. S5). It was of similar size (33 nm) and morphology (Fig. 6A) to **1c**@ and DiR/**1c**@, and displayed similar NIRF (Fig. S6) and ^{19}F-MRI properties (Tab. S2, Fig. 6B and 6C). Importantly also, PTX/DiR/**1c**@ and PTX/**1c**@ produced similar T_2 values to **1c**@ (Tab. S2), indicating a lack of effect of PTX encapsulation on the mobility of the fluorine nuclei on the dendrimer surface. The high drug loading and the retained favorable relaxation properties made PTX/DiR/**1c**@ particularly appealing for use in ^{19}F-MRI-based multimodality imaging and theranostics.

We performed multimodal imaging for cancer detection and assessed the theranostics capacity of PTX/DiR/**1c**@ using L-IPC-xenograft mice. Specifically, we intravenously injected PTX/DiR/**1c**@ into L-IPC-xenograft mice on days 0, 4, 7 and 11 at the PTX equivalent dose of 7.5 mg/kg. NIRF imaging indicated the presence of PTX/DiR/**1c**@ at the tumor sites (Fig. 6D) on day 2. ^{19}F-MRI signals were also observed in the tumors (Fig. 6E), confirming the performance of PTX/DiR/**1c**@ as a dual ^{19}F-MRI and NIRF imaging agent. Furthermore, mice treated with PTX/DiR/**1c**@ showed markedly inhibited tumor growth, compared to a non-significant inhibition in those treated with the equivalent dose of PTX only (Fig. 6F). Effective anticancer activity was further confirmed using PTX/**1c**@ at an even lower PTX dose of 3.0 mg/kg (Fig. 6G). The superior anticancer activities of both PTX/**1c**@ and PTX/DiR/**1c**@ over the free drug PTX can be ascribed to the EPR-based passive tumor targeting that is permitted through encapsulation of the drug within the nanoparticles. The resulting increased accumulation and local concentration of drug within the tumor achieves better and more efficacious treatment.

To investigate the mechanism involved in the observed inhibition of tumor growth, we used Ki-67 staining, TUNEL, and Caspase-3 activation assays to respectively asses cancer cell proliferation, apoptosis induction, and caspase activation in tumor tissue following treatment with PTX/**1c**@. Tumor tissues from mice treated with PTX/**1c**@ displayed considerably fewer Ki-67 positive cells (Fig. 6H) but many more TUNEL positive cells (Fig. 6I) and activated caspase-3 positive cells (Fig. 6J) compared to those treated with the PBS control, PTX alone or **1c**@ alone. These results offer compelling evidence in favor of PTX/**1c**@ providing an effective antiproliferative tumor suppressing effect *in vivo* brought about by the induction of caspase-dependent apoptosis.

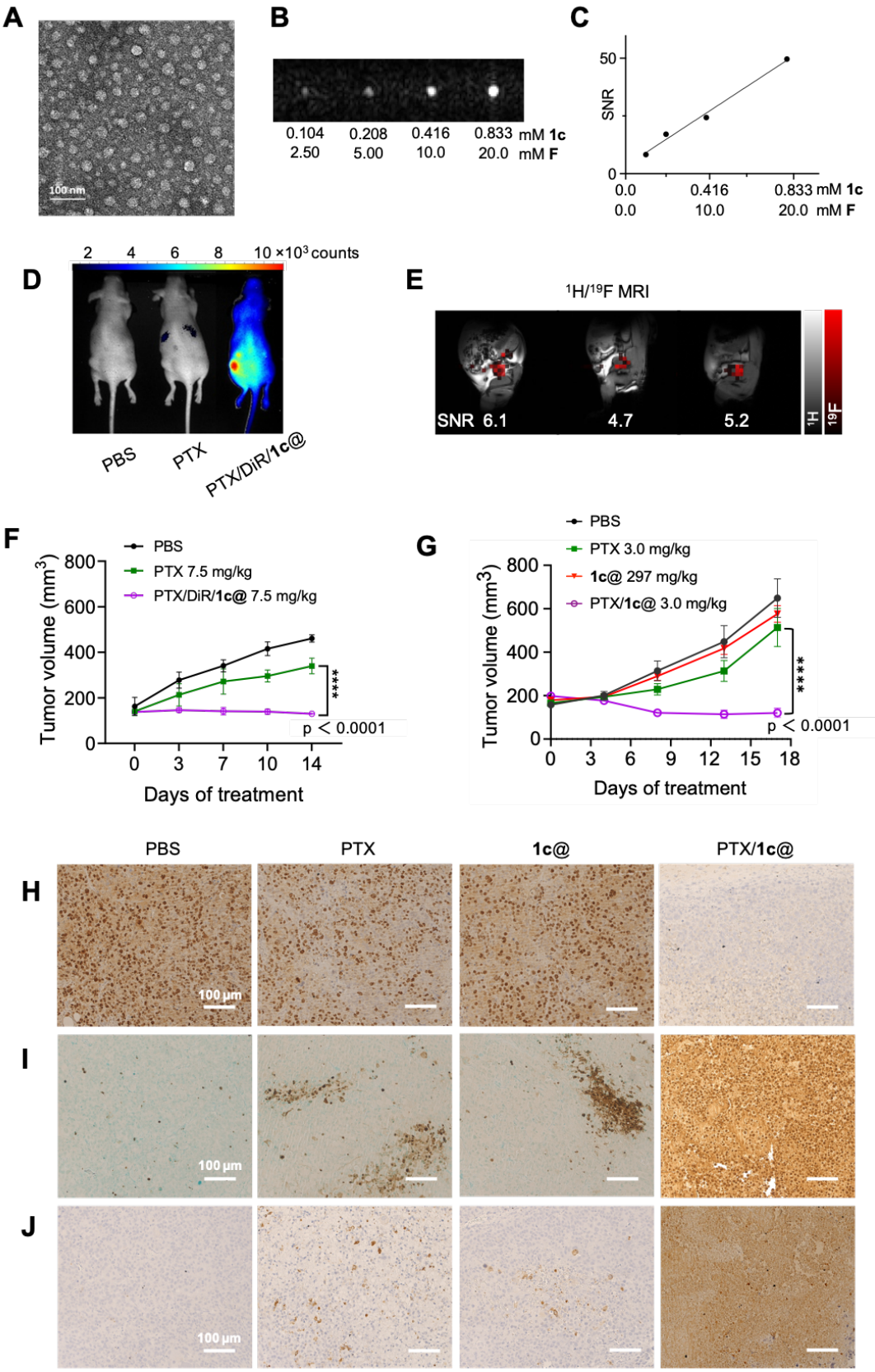

Fig. 6 Paclitaxel (PTX) delivered in PTX/DiR/**1c**@ and PTX/**1c**@ nanoprobes for ^{19}F-MRI-based multimodal imaging and theranostics for tumor detection and treatment. (A) Transmission electron microscopic image of PTX/DiR/**1c**@. (B) Fluorine magnetic resonance imaging (^{19}F-MRI) of

PTX/DiR/**1c**@ at 7 T at various concentrations of **1c** and fluorine. (C) ^{19}F-MRI signal-to-noise ratio (SNR) of PTX/DiR/**1c**@ increasing linearly as the concentrations of **1c** and fluorine increases. (D) Fluorescence imaging 48 h after the first injection. (E) ^{19}F-MRI superimposed on anatomic ^{1}H-MRI of tumors in three different L-IPC xenograft mice 48 h after the last injection of PTX/DiR/**1c**@. Intravenous injection of PTX/DiR/**1c**@ (DiR: 80 μg/kg; **1c**: 0.21 mmol/kg; PTX: 7.5 mg/kg) twice per week for 2 weeks. MR images were acquired in the sagittal plane with respect to the mouse. (F, G) Tumor growth inhibition in L-IPC xenograft mice following intravenous injection of (F) PTX/DiR/**1c**@ at a PTX concentration of 7.5 mg/kg (n = 3 per group) or (G) PTX/**1c**@ at a PTX concentration of 3.0 mg/kg (n= 5 per group) twice per week for 2 weeks. Statistical differences were assessed using two-way ANOVA with Tukey's multiple comparison test. ****: $p \leq 0.0001$. (H) Ki-67, (I) TUNEL assay, and (J) Cleaved caspase-3 immunohistochemistry staining analysis results for tumor sections from mice treated with PBS, PTX (3.0 mg/kg), **1c**@ (**1c**: 0.21 mmol/kg), and PTX/**1c**@ (PTX: 3.0 mg/kg; **1c**: 0.2 mmol/kg) (scale bar = 100 μm).

It is important to note that all mice tolerated the treatment well and showed no detectable side-effect. None displayed any abnormal behavior or marked change in body weight (Fig. S7) throughout the treatment period, nor any pathological signs in the main organs on histology (Fig. S8). Collectively, our results demonstrate that PTX/**1c**@ nanomicelles are safe and effective for use as theranostics to detect and treat cancer.

Conclusion

In this study, we have developed innovative self-assembling fluorinated dendrimer nanosystems for effective ^{19}F-MRI, ^{19}F-MRI-based multimodal imaging and theranostics for cancer imaging and treatment. Incorporating charged moieties adjacent to the fluorine moieties at the dendrimer terminals permitted fluorine nuclei mobility while retaining a high fluorine content with a good degree of water solubility. The resulting fluorinated nanosystem displayed favorable relaxation properties for effective ^{19}F-MRI. Importantly, the encapsulation of a pharmaceutical agent within the self-assembling supramolecular dendrimer core did not affect the relaxation properties of ^{19}F nuclei located on the surface of the nanoparticle; the two were sufficiently segregated in space to avoid interference.

Specifically, in this study, we used the fluorescence dye DiR and the anticancer drug PTX as model pharmaceutical agents to demonstrate the effectiveness of multimodal ^{19}F-MRI and NIRF imaging and theranostics achievable with our modular nanosystems for the simultaneous detection and treatment of cancer, in this case a pancreatic cancer patient-derived xenograft model. In particular, our nanosystems, whether PTX/DiR/**1c**@ or PTX/**1c**@, enabled effective and potent anticancer activity compared with PTX alone, which achieved no significant anticancer effect. This can be ascribed to the passive tumor targeting by PTX/DiR/**1c**@ and PTX/**1c**@ both exploiting the EPR-effect unique to the tumor microenvironment for nanotechnology-based drug delivery.

For the future in personalized medicine, the approach that we have demonstrated can be adapted to the construction of modular nanosystems for desired multimodal imaging and theranostics, enabling targeted delivery of patient-specific pharmaceutical agents and imaging feedback of their effects.

This concept of modular nanosystems issued from self-assembling supramolecular dendrimers has provided an innovative new approach to creating a platform offering both imaging agents for various ^{19}F-MRI-based biomedical applications and multimodal theranostic agents for more efficient treatment and treatment monitoring. We are actively pursuing in this direction.

Author contributions

LP conceived and coordinated the project; ZL and BR synthesized the agents; ZL, BR, LD, TR, AT, SG, TAPB, EL and SP performed the characterization; JI provided the animal model; BR, LD, YJ, BL, XL, and ZL performed the animal experiments; LD, BL, and CG assessed toxicity; TAPB, AV, ZL, BR, LD, YJ, and XL performed in vivo imaging experiments; ZL, BR, LD, YJ, BL, XL, XXL, TAPB, AV, MB, EL, SP and LP analyzed the data; ZL, BR, CG, BL, XL, TAPB, AV, MB, EL, SP and LP wrote the paper. All authors proofed the manuscript.

Acknowledgements

This work was supported by the Ligue Nationale Contre le Cancer (EL2016, EL2021 LNCCLiP, LP; doctoral fellowship grant, ZL), the French National Research Agency under the framework of the ERA-NET EURONANOMED European Research project 'NAN-4-TUM' (LP), the EU H2020 Research and Innovation program NMBP "SAFE-N-MEDTECH" (2019-2023) (grant agreement No. 814607, LP, BR, TR, XXL), the EU Horizon Europe Research and Innovation program Cancer Mission "HIT-GLIO" (2023-2027) (grant agreement No. 101136835, LP), and China Scholarship Council (LD, XL). The relaxometric and preclinical MRI studies were performed at CRMBM, which is a member of France Life Imaging (grant ANR-11-INBS-0006 from the French "Investissements d'Avenir" program). EL and SP acknowledge the financial support from the Italian Association for Cancer Research (AIRC, IG17413), and the ICSC-Centro Nazionale di Ricerca in High-performance computing, big data, and quantum computing (Spoke 7, WP4 (Pilot applications), T.2.8 (Development and optimization of HPC-based integrated workflows based on flagship codes for personalized (nano)medicine) and CINECA, funded by European Union – NextGenerationEU.

References:

1. Harisinghani, M. G.; O' Shea, A.; Weissleder, R., Advances in clinical MRI technology. *Sci. Transl. Med.* **2019,** *11* (523), eaba2591.

2. Terreno, E.; Castelli, D. D.; Viale, A.; Aime, S., Challenges for Molecular Magnetic Resonance Imaging. *Chem. Rev.* **2010,** *110* (5), 3019-3042.

3. Wahsner, J.; Gale, E. M.; Rodriguez-Rodriguez, A.; Caravan, P., Chemistry of MRI Contrast Agents: Current Challenges and New Frontiers. *Chem. Rev.* **2019,** *119* (2), 957-1057.

4. Tirotta, I.; Dichiarante, V.; Pigliacelli, C.; Cavallo, G.; Terraneo, G.; Bombelli, F. B.; Metrangolo, P.; Resnati, G., ^{19}F magnetic resonance imaging (MRI): from design of materials to clinical applications. *Chem. Rev.* **2015,** *115* (2), 1106-29.

5. Janasik, D.; Krawczyk, T., ^{19}F MRI Probes for Multimodal Imaging. *Chemistry (Easton)* **2022,** *28* (5), e202102556.

6. Zhang, C.; Yan, K.; Fu, C.; Peng, H.; Hawker, C. J.; Whittaker, A. K., Biological Utility of Fluorinated Compounds: from Materials Design to Molecular Imaging, Therapeutics and Environmental Remediation. *Chem. Rev.* **2022,** *122* (1), 167-208.
7. Krafft, M. P.; Riess, J. G., Chemistry, Physical Chemistry, and Uses of Molecular Fluorocarbon−Hydrocarbon Diblocks, Triblocks, and Related Compounds—Unique "Apolar" Components for Self-Assembled Colloid and Interface Engineering. *Chem. Rev.* **2009,** *109* (5), 1714-1792.
8. Jirak, D.; Galisova, A.; Kolouchova, K.; Babuka, D.; Hruby, M., Fluorine polymer probes for magnetic resonance imaging: quo vadis? *MAGMA* **2019,** *32* (1), 173-185.
9. Peng, Q.; Li, Y.; Bo, S.; Yuan, Y.; Yang, Z.; Chen, S.; Zhou, X.; Jiang, Z. X., Paramagnetic nanoemulsions with unified signals for sensitive ^{19}F MRI cell tracking. *Chem. Commun. (Camb.)* **2018,** *54* (47), 6000-6003.
10. Jahromi, A. H.; Wang, C.; Adams, S. R.; Zhu, W.; Narsinh, K.; Xu, H.; Gray, D. L.; Tsien, R. Y.; Ahrens, E. T., Fluorous-Soluble Metal Chelate for Sensitive Fluorine-19 Magnetic Resonance Imaging Nanoemulsion Probes. *ACS Nano* **2019,** *13* (1), 143-151.
11. Schmieder, A. H.; Caruthers, S. D.; Keupp, J.; Wickline, S. A.; Lanza, G. M., Recent Advances in ^{19}Fluorine Magnetic Resonance Imaging with Perfluorocarbon Emulsions. *Engineering (Beijing)* **2015,** *1* (4), 475-489.
12. Wang, K.; Peng, H.; Thurecht, K. J.; Puttick, S.; Whittaker, A. K., Segmented Highly Branched Copolymers: Rationally Designed Macromolecules for Improved and Tunable ^{19}F MRI. *Biomacromolecules* **2015,** *16* (9), 2827-2839.
13. J. Thurecht, K.; Blakey, I.; Peng, H.; Squires, O.; Hsu, S.; Alexander, C.; K. Whittaker, A., Functional hyperbranched polymers: toward targeted *in Vivo* ^{19}F magnetic resonance imaging using designed macromolecules. *J. Am. Chem. Soc.* **2010,** *132*, 5336-5337.
14. Du, W.; Nyström, A. M.; Zhang, L.; Powell, K. T.; Li, Y.; Cheng, C.; Wickline, S. A.; Wooley, K. L., Amphiphilic Hyperbranched Fluoropolymers as Nanoscopic ^{19}F Magnetic Resonance Imaging Agent Assemblies. *Biomacromolecules* **2008,** *9* (10), 2826-2833.
15. Huang, Z.; Sengar, R. S.; Nigam, A.; Abadjian, M.-C.; Potter, D. M.; Grotjahn, D. B.; Wiener, E. C., A fluorinated dendrimer-based nanotechnology platform new contrast agents for high field imaging. *Invest. Radiol.* **2010,** *45* (10), 641–654.
16. Yue, X.; Taraban, M. B.; Hyland, L. L.; Yu, Y. B., Avoiding steric congestion in dendrimer growth through proportionate branching: a twist on da Vinci's rule of tree branching. *J. Org. Chem.* **2012,** *77* (20), 8879-87.
17. Yu, W.; Yang, Y.; Bo, S.; Li, Y.; Chen, S.; Yang, Z.; Zheng, X.; Jiang, Z.-X.; Zhou, X., Design and Synthesis of Fluorinated Dendrimers for Sensitive 19F MRI. *The Journal of Organic Chemistry* **2015,** *80* (9), 4443-4449.
18. Criscione, J. M.; Le, B. L.; Stern, E.; Brennan, M.; Rahner, C.; Papademetris, X.; Fahmy, T. M., Self-assembly of pH-responsive fluorinated dendrimer-based particulates for drug delivery and noninvasive imaging. *Biomaterials* **2009,** *30* (23-24), 3946-55.
19. Ogawa, M.; Nitahara, S.; Aoki, H.; Ito, S.; Narazaki, M.; Matsuda, T., Synthesis and Evaluation of Water-Soluble Fluorinated Dendritic Block-Copolymer Nanoparticles as a 19F-MRI Contrast Agent. *Macromol. Chem. Phys.* **2010,** *211* (14), 1602-1609.
20. Huang, X.; Huang, G.; Zhang, S.; Sagiyama, K.; Togao, O.; Ma, X.; Wang, Y.; Li, Y.; Soesbe, T. C.; Sumer, B. D.; Takahashi, M.; Sherry, A. D.; Gao, J., Multi-chromatic pH-activatable ^{19}F-MRI

nanoprobes with binary ON/OFF pH transitions and chemical-shift barcodes. *Angew. Chem. Int. Ed. Engl.* **2013,** *52* (31), 8074-8.

21. Kirberger, S. E.; Maltseva, S. D.; Manulik, J. C.; Einstein, S. A.; Weegman, B. P.; Garwood, M.; Pomerantz, W. C. K., Synthesis of Intrinsically Disordered Fluorinated Peptides for Modular Design of High-Signal ^{19}F MRI Agents. *Angew. Chem. Int. Ed.* **2017,** *56* (23), 6440-6444.

22. Munkhbat, O.; Canakci, M.; Zheng, S.; Hu, W.; Osborne, B.; Bogdanov, A. A.; Thayumanavan, S., ^{19}F MRI of Polymer Nanogels Aided by Improved Segmental Mobility of Embedded Fluorine Moieties. *Biomacromolecules* **2019,** *20* (2), 790-800.

23. Wang, K.; Peng, H.; Thurecht, K. J.; Puttick, S.; Whittaker, A. K., pH-responsive star polymer nanoparticles: potential ^{19}F MRI contrast agents for tumour-selective imaging. *Polymer Chemistry* **2013,** *4* (16), 4480-4489.

24. Garrigue, P.; Tang, J.; Ding, L.; Bouhlel, A.; Tintaru, A.; Laurini, E.; Huang, Y.; Lyu, Z.; Zhang, M.; Fernandez, S.; Balasse, L.; Lan, W.; Mas, E.; Marson, D.; Weng, Y.; Liu, X.; Giorgio, S.; Iovanna, J.; Pricl, S.; Guillet, B.; Peng, L., Self-assembling supramolecular dendrimer nanosystem for PET imaging of tumors. *Proceedings of the National Academy of Sciences* **2018,** *115* (45), 11454-11459.

25. Ding, L.; Lyu, Z.; Louis, B.; Tintaru, A.; Laurini, E.; Marson, D.; Zhang, M.; Shao, W.; Jiang, Y.; Bouhlel, A.; Balasse, L.; Garrigue, P.; Mas, E.; Giorgio, S.; Iovanna, J.; Huang, Y.; Pricl, S.; Guillet, B.; Peng, L., Bioimaging: Surface Charge of Supramolecular Nanosystems for In Vivo Biodistribution: A MicroSPECT/CT Imaging Study (Small 37/2020). *Small* **2020,** *16* (37), 2070203.

26. Ding, L.; Lyu, Z.; Tintaru, A.; Laurini, E.; Marson, D.; Louis, B.; Bouhlel, A.; Balasse, L.; Fernandez, S.; Garrigue, P.; Mas, E.; Giorgio, S.; Pricl, S.; Guillet, B.; Peng, L., A self-assembling amphiphilic dendrimer nanotracer for SPECT imaging. *Chem. Commun.* **2020,** *56* (2), 301-304.

27. Ding, L.; Lyu, Z.; Perles-Barbacaru, T.-A.; Huang, A. Y.-T.; Lian, B.; Jiang, Y.; Roussel, T.; Galanakou, C.; Giorgio, S.; Kao, C.-L.; Liu, X.; Iovanna, J.; Bernard, M.; Viola, A.; Peng, L., Modular self-assembling dendrimer nanosystems for magnetic resonance and multimodality imaging of tumors. *Adv. Mater.* **2023,** *DOI: 10.1002/adma.202308262*.

28. Matsumura, Y.; Maeda, H., A new concept for macromolecular therapeutics in cancer chemotherapy: mechanism of tumoritropic accumulation of proteins and the antitumor agent smancs. *Cancer Res.* **1986,** *46* (12 Pt 1), 6387-92.

29. Gerlowski, L. E.; Jain, R. K., Microvascular permeability of normal and neoplastic tissues. *Microvasc. Res.* **1986,** *31* (3), 288-305.

30. Maeda, H., Toward a full understanding of the EPR effect in primary and metastatic tumors as well as issues related to its heterogeneity. *Adv Drug Deliv Rev* **2015,** *91*, 3-6.

31. Sun, R.; Xiang, J.; Zhou, Q.; Piao, Y.; Tang, J.; Shao, S.; Zhou, Z.; Bae, Y. H.; Shen, Y., The tumor EPR effect for cancer drug delivery: Current status, limitations, and alternatives. *Adv Drug Deliv Rev* **2022,** *191*, 114614.

32. Percec, V.; Wilson, D. A.; Leowanawat, P.; Wilson, C. J.; Hughes, A. D.; Kaucher, M. S.; Hammer, D. A.; Levine, D. H.; Kim, A. J.; Bates, F. S.; Davis, K. P.; Lodge, T. P.; Klein, M. L.; DeVane, R. H.; Aqad, E.; Rosen, B. M.; Argintaru, A. O.; Sienkowska, M. J.; Rissanen, K.; Nummelin, S.; Ropponen, J., Self-Assembly of Janus Dendrimers into Uniform Dendrimersomes and Other Complex Architectures. *Science* **2010,** *328* (5981), 1009-1014.

33. Lyu, Z.; Ding, L.; Tintaru, A.; Peng, L., Self-Assembling Supramolecular Dendrimers for Biomedical Applications: Lessons Learned from Poly(amidoamine) Dendrimers. *Acc. Chem. Res.* **2020,** *53* (12), 2936-2949.

34. Chen, J.; Zhu, D.; Liu, X.; Peng, L., Amphiphilic Dendrimer Vectors for RNA Delivery: State-of-the-Art and Future Perspective. *Accounts of materials research* **2022,** *3* (5), 484-497.
35. Yu, T.; Liu, X.; Bolcato-Bellemin, A.-L.; Wang, Y.; Liu, C.; Erbacher, P.; Qu, F.; Rocchi, P.; Behr, J.-P.; Peng, L., An Amphiphilic Dendrimer for Effective Delivery of Small Interfering RNA and Gene Silencing In Vitro and In Vivo. *Angew. Chem. Int. Ed.* **2012,** *51* (34), 8478-8484.
36. Dhumal, D.; Maron, B.; Malach, E.; Lyu, Z.; Ding, L.; Marson, D.; Laurini, E.; Tintaru, A.; Ralahy, B.; Giorgio, S.; Pricl, S.; Hayouka, Z.; Peng, L., Dynamic self-assembling supramolecular dendrimer nanosystems as potent antibacterial candidates against drug-resistant bacteria and biofilms. *Nanoscale* **2022,** *14* (26), 9286-9296.
37. Laurini, E.; Aulic, S.; Skoko, N.; Marson, D.; Fermeglia, M.; Pricl, S., ITC for Characterization of Self-Assembly Process of Cationic Dendrons for siRNA Delivery. In *Design and Delivery of SiRNA Therapeutics*, Ditzel, H. J.; Tuttolomondo, M.; Kauppinen, S., Eds. Springer US: New York, NY, 2021; pp 245-266.
38. Russi, M.; Valeri, R.; Marson, D.; Danielli, C.; Felluga, F.; Tintaru, A.; Skoko, N.; Aulic, S.; Laurini, E.; Pricl, S., Some things old, new and borrowed: Delivery of dabrafenib and vemurafenib to melanoma cells via self-assembled nanomicelles based on an amphiphilic dendrimer. *Eur. J. Pharm. Sci.* **2023,** *180*, 106311.
39. Kleeff, J.; Korc, M.; Apte, M.; La Vecchia, C.; Johnson, C. D.; Biankin, A. V.; Neale, R. E.; Tempero, M.; Tuveson, D. A.; Hruban, R. H.; Neoptolemos, J. P., Pancreatic cancer. *Nature Reviews Disease Primers* **2016,** *2* (1), 16022.
40. Christenson, E. S.; Jaffee, E.; Azad, N. S., Current and emerging therapies for patients with advanced pancreatic ductal adenocarcinoma: a bright future. *Lancet Oncol.* **2020,** *21* (3), e135-e145.
41. Garg, S. K.; Chari, S. T., Early detection of pancreatic cancer. *Current opinion in gastroenterology* **2020,** *36* (5), 456-461.
42. Liu, J.; Chen, C.; Wei, T.; Gayet, O.; Loncle, C.; Borge, L.; Dusetti, N.; Ma, X.; Marson, D.; Laurini, E.; Pricl, S.; Gu, Z.; Iovanna, J.; Peng, L.; Liang, X.-J., Dendrimeric nanosystem consistently circumvents heterogeneous drug response and resistance in pancreatic cancer. *Exploration* **2021,** *1* (1), 21-34.
43. Hosein, A. N.; Brekken, R. A.; Maitra, A., Pancreatic cancer stroma: an update on therapeutic targeting strategies. *Nat. Rev. Gastroenterol. Hepatol.* **2020,** *17* (8), 487-505.
44. Wang, K.; Du, Y.; Zhang, Z.; He, K.; Cheng, Z.; Yin, L.; Dong, D.; Li, C.; Li, W.; Hu, Z.; Zhang, C.; Hui, H.; Chi, C.; Tian, J., Fluorescence image-guided tumour surgery. *Nature Reviews Bioengineering* **2023,** *1* (3), 161-179.
45. Hong, G.; Antaris, A. L.; Dai, H., Near-infrared fluorophores for biomedical imaging. *Nature Biomedical Engineering* **2017,** *1* (1), 0010.
46. Gawne, P. J.; Ferreira, M.; Papaluca, M.; Grimm, J.; Decuzzi, P., New opportunities and old challenges in the clinical translation of nanotheranostics. *Nature Reviews Materials* **2023,** *8* (12), 783-798.
47. Chen, H.; Zhang, W.; Zhu, G.; Xie, J.; Chen, X., Rethinking cancer nanotheranostics. *Nature Reviews Materials* **2017,** *2* (7), 17024.
48. Jiang, Y.; Lyu, Z.; Ralahy, B.; Liu, J.; Roussel, T.; Ding, L.; Tang, J.; Kosta, A.; Giorgio, S.; Tomasini, R.; Liang, X. J.; Dusetti, N.; Iovanna, J.; Peng, L., Dendrimer nanosystems for adaptive tumor-assisted drug delivery via extracellular vesicle hijacking. *Proc. Natl. Acad. Sci. U. S. A.* **2023,** *120* (7),

e2215308120.
49. Wei, T.; Chen, C.; Liu, J.; Liu, C.; Posocco, P.; Liu, X.; Cheng, Q.; Huo, S.; Liang, Z.; Fermeglia, M.; Pricl, S.; Liang, X. J.; Rocchi, P.; Peng, L., Anticancer drug nanomicelles formed by self-assembling amphiphilic dendrimer to combat cancer drug resistance. *Proc. Natl. Acad. Sci. U. S. A.* **2015,** *112* (10), 2978-83.

Supporting Information For

Self-assembling dendrimers for fluorine magnetic resonance imaging (^{19}F-MRI) and ^{19}F-MRI-based multimodal imaging and theranostics

Zhenbin LYU[1,2,#], Brigino RALAHY[1,#], Teodora-Adriana PERLES-BARBACARU[3,#], Ling DING[1,3,#], Yifan JIANG[1], Baoping LIAN[4], Tom ROUSSEL[1], Xi LIU[1,5], Christina GALANAKOU[1], Erik LAURINI[6], Aura TINTARU[2], Suzanne GIORGIO[1], Sabrina PRICL[6,7], Xiaoxuan LIU[4], Monique BERNARD[3], Juan IOVANNA[5], Angèle VIOLA[3], Ling PENG[1,*]

[1] Aix Marseille University, CNRS, Centre Interdisciplinaire de Nanoscience de Marseille (CINaM), UMR 7325, Equipe Labellisée Ligue Contre le Cancer, 13288 Marseille, France

[2] Aix Marseille University, CNRS, Institut de Chimie Radicalaire (ICR), UMR 7273, 13013 Marseille, France

[3] Aix Marseille University, CNRS, Centre de Résonance Magnétique Biologique et Médicale (CRMBM), UMR 7339, 13385 Marseille, France

[4] State Key Laboratory of Natural Medicines and Jiangsu Key Laboratory of Drug Discovery for Metabolic Diseases, Center of Drug Discovery, Center of Advanced Pharmaceuticals and Biomaterials, China Pharmaceutical University, 431007 Nanjing, P. R. China

[5] Centre de Recherche en Cancérologie de Marseille, INSERM U1068, CNRS, UMR 7258, Institut Paoli-Calmettes, Aix Marseille Université, 13273 Marseille, France

[6] Molecular Biology and Nanotechnology Laboratory (MolBNL@UniTS), DEA, University of Trieste, 34127 Trieste, Italy

[7] Department of General Biophysics, Faculty of Biology and Environmental Protection, University of Lodz, 90-236 Lodz, Poland

[#] These authors contributed equally

[*] ling.peng@univ-amu.fr

Table of Content

Tab. S1. Molecular weight, fluorine number, fluorine content and critical micelle concentration (CMC) of **1a-c**

Dendrimer	Molecular weight	Fluorine number	Fluorine content (wt%)	CMC (μM)
1a	772.9	6	14.8	35
1b	1423.5	12	16.0	29
1c	2724.6	24	16.7	120

Tab. S2. Relaxation properties of the self-assembling dendrimer nanosystems **1c**@, DiR/**1c**@, PTX/DiR/**1c**@ and PTX/**1c**@ at different fluorine concentrations, assessed using an MRI scanner at 7T. Best-fit values (95% confidence intervals of the fits) are given.

Dendrimer nanosystem	2.50 mM **F**		10.0 mM **F**	
	$\mathbf{T_1}$ (ms)	$\mathbf{T_2}$ (ms)	$\mathbf{T_1}$ (ms)	$\mathbf{T_2}$ (ms)
1c@	550 (341-822)	426 (411-441)	588 (441-771)	226 (218-234)
DiR/**1c**@	473 (375-590)	445 (421-470)	621 (523-733)	237 (230-243)
PTX/DiR/**1c**@	490 (367-637)	270 (262-279)	497 (471-523)	181 (172-191)
PTX/**1c**@	560 (442-699)	403 (391-416)	482 (438-528)	180 (177-184)

Fig. S1. Synthesis of **1a** (A), **1b** (B) and **1c** (C).

A

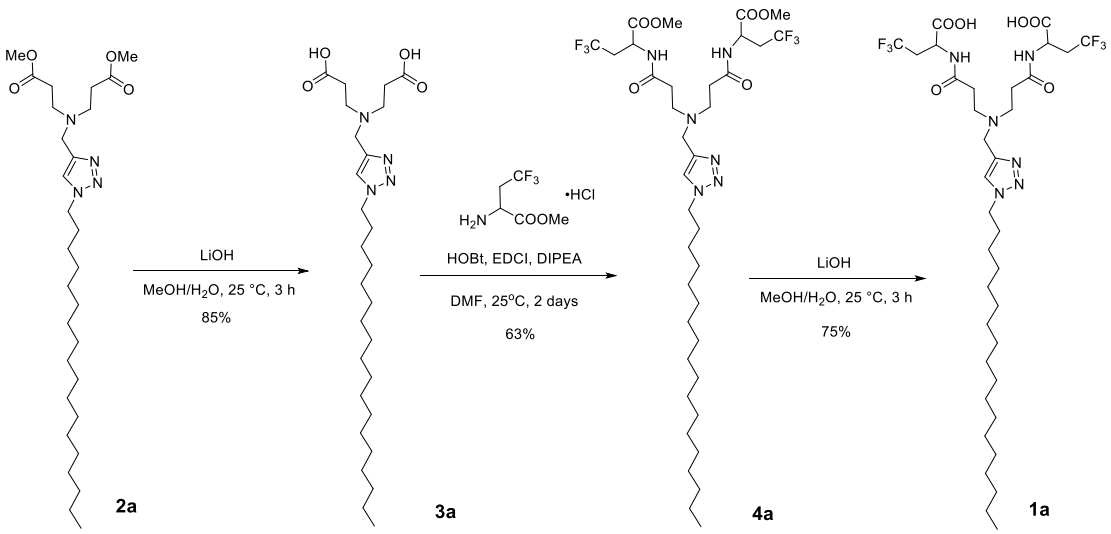

B

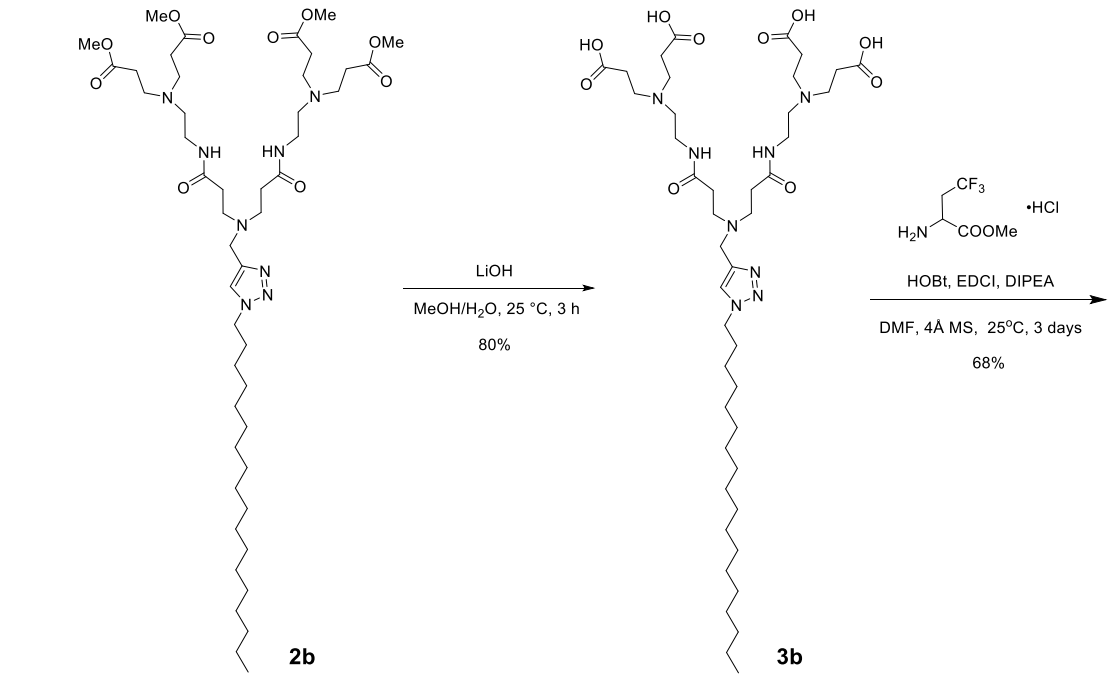
LiOH
MeOH/H2O, 25 °C, 3 h
80%
HOBt, EDCI, DIPEA
DMF, 4Å MS, 25°C, 3 days
68%
•HCl
2b
3b

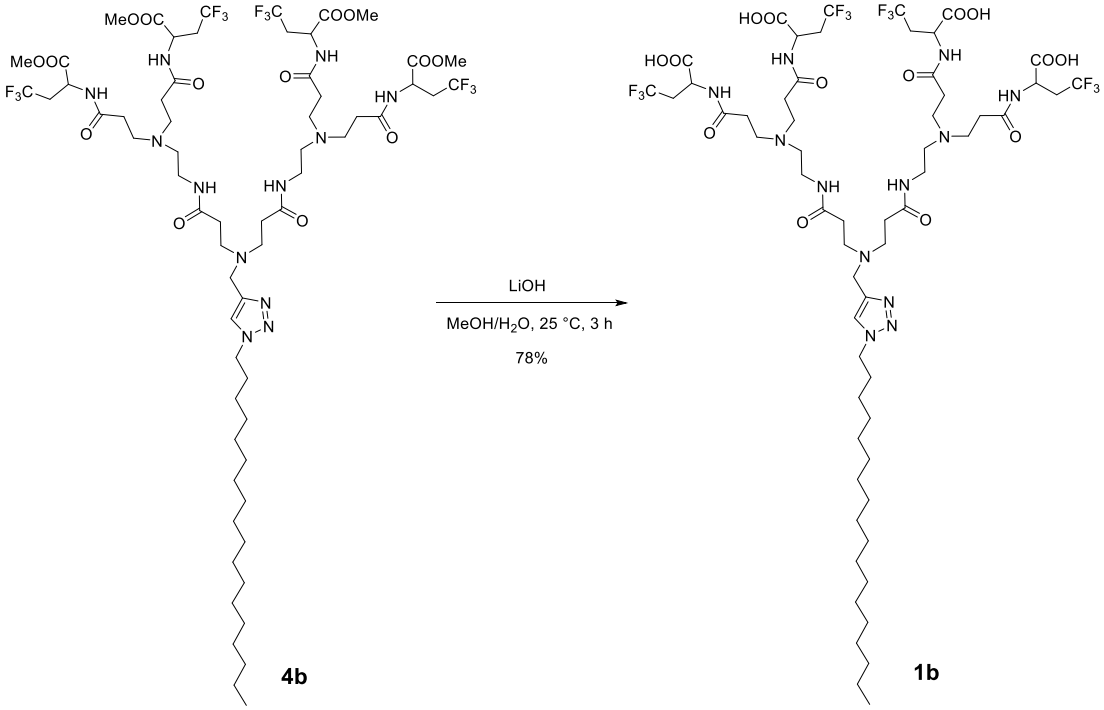
LiOH
MeOH/H2O, 25 °C, 3 h
78%
4b
1b

C

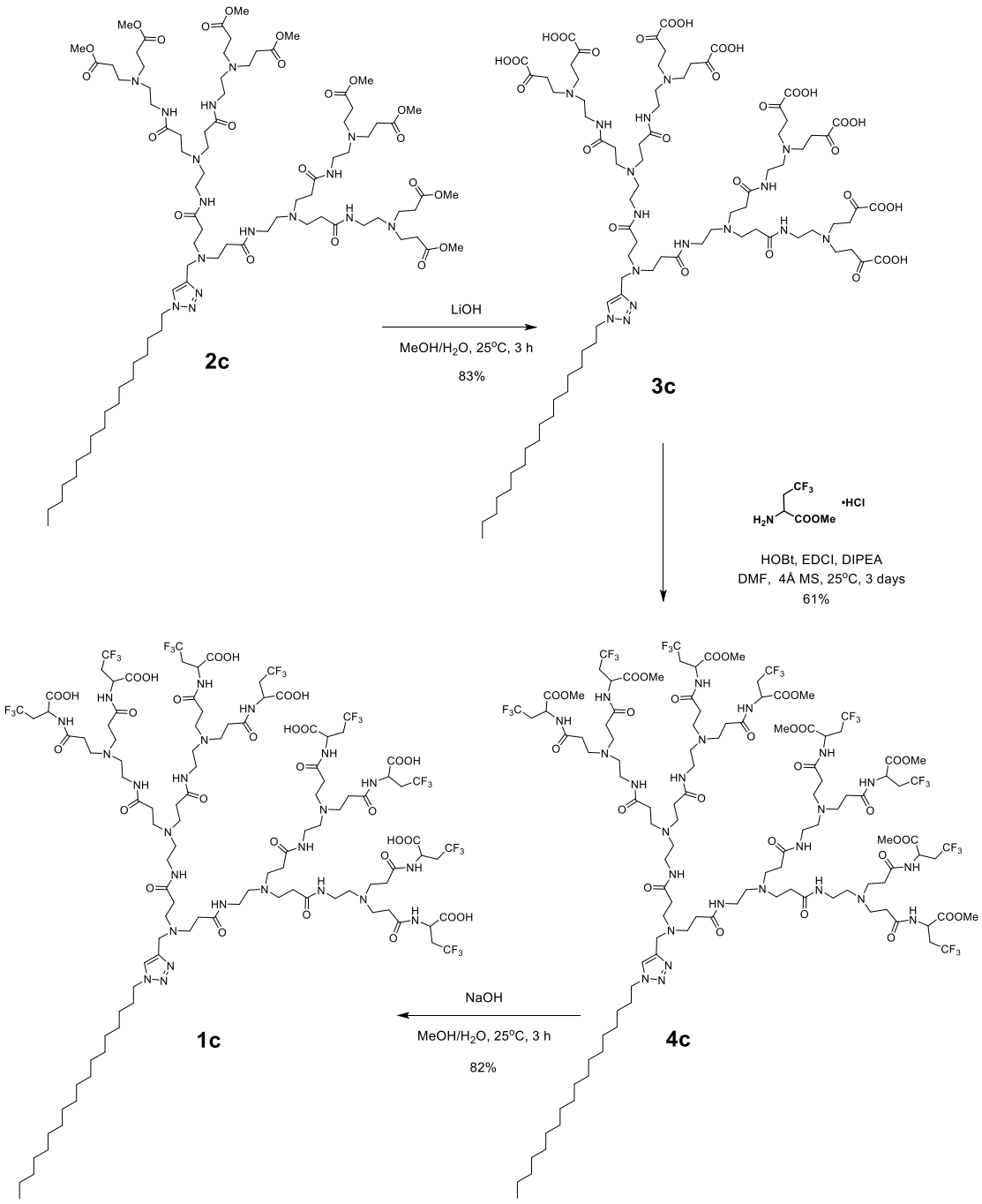
2c
LiOH
MeOH/H2O, 25°C, 3 h
83%
3c
•HCl
HOBt, EDCI, DIPEA
DMF, 4Å MS, 25°C, 3 days
61%
1c
NaOH
MeOH/H2O, 25°C, 3 h
82%
4c

Fig. S2. ^{1}H- and ^{13}C-NMR spectra of **1a** (A,B), **1b** (C,D) and **1c** (E,F).

A. ^{1}H NMR of **1a** (400 MHz, CD_3OD)

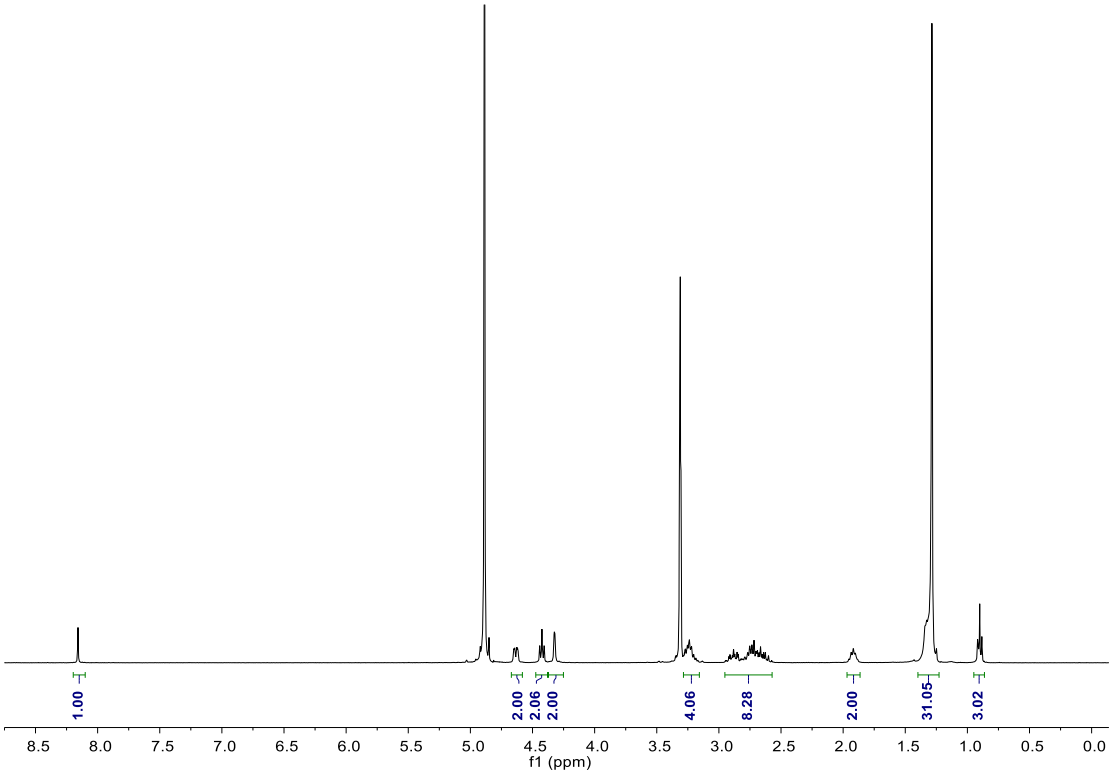

B. ^{13}C NMR of **1a** (101 MHz, $CD_3OD/CDCl_3$=1/1)

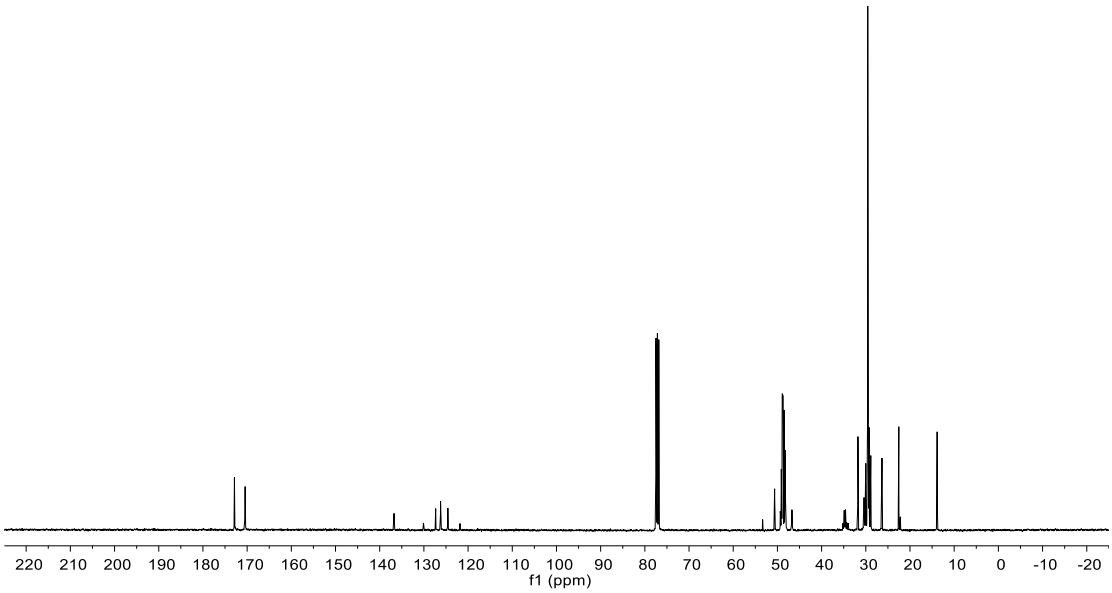

C. ^{1}H NMR of **1b** (400 MHz, CD_3OD)

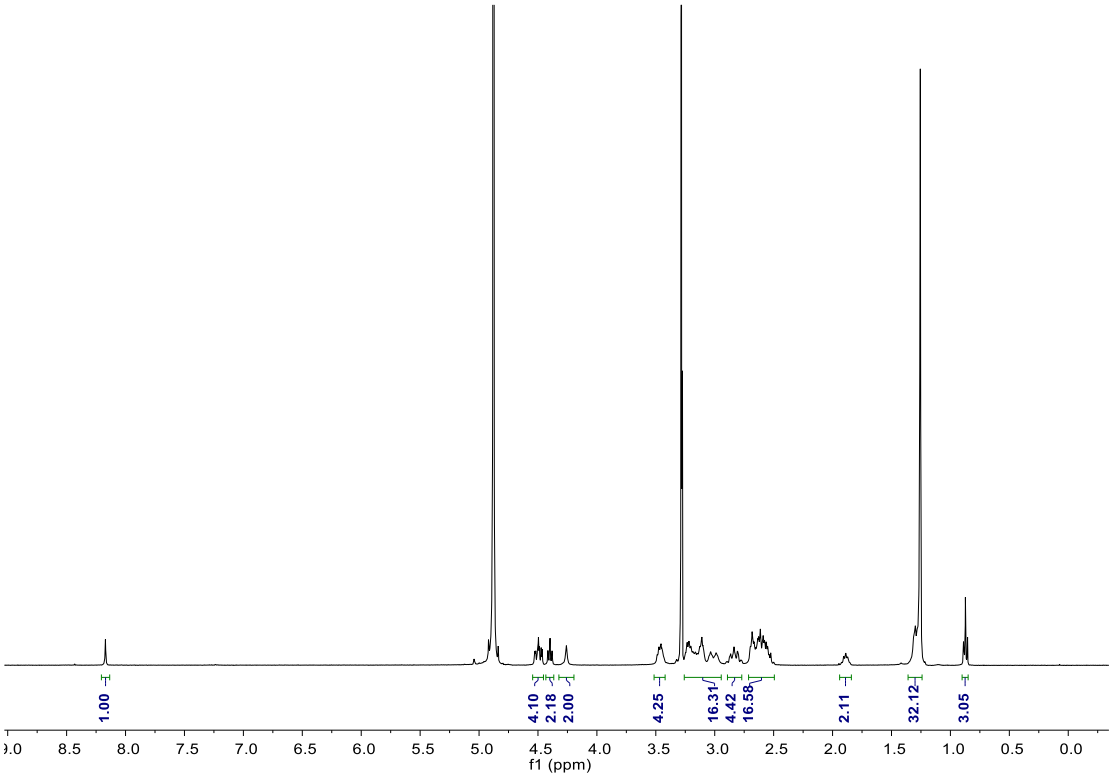

D. ^{13}C NMR of **1b** (101 MHz, CD_3OD)

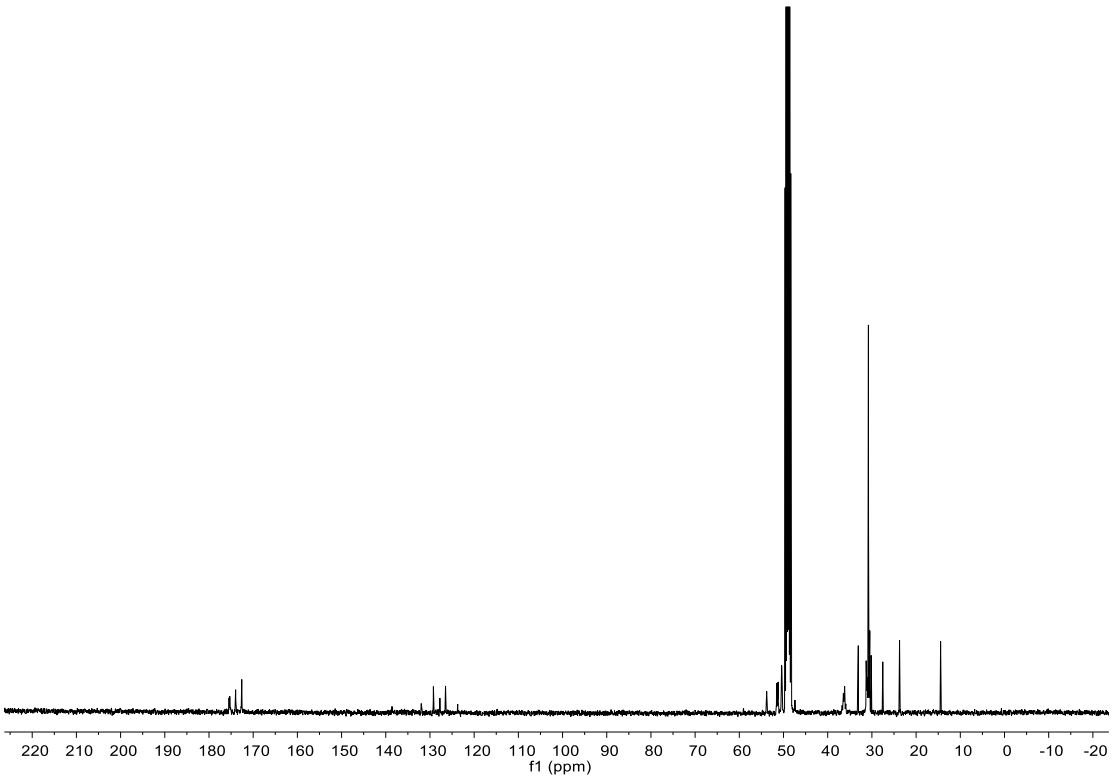

E. ^{1}H NMR of **1c** (400 MHz, CD_3OD)

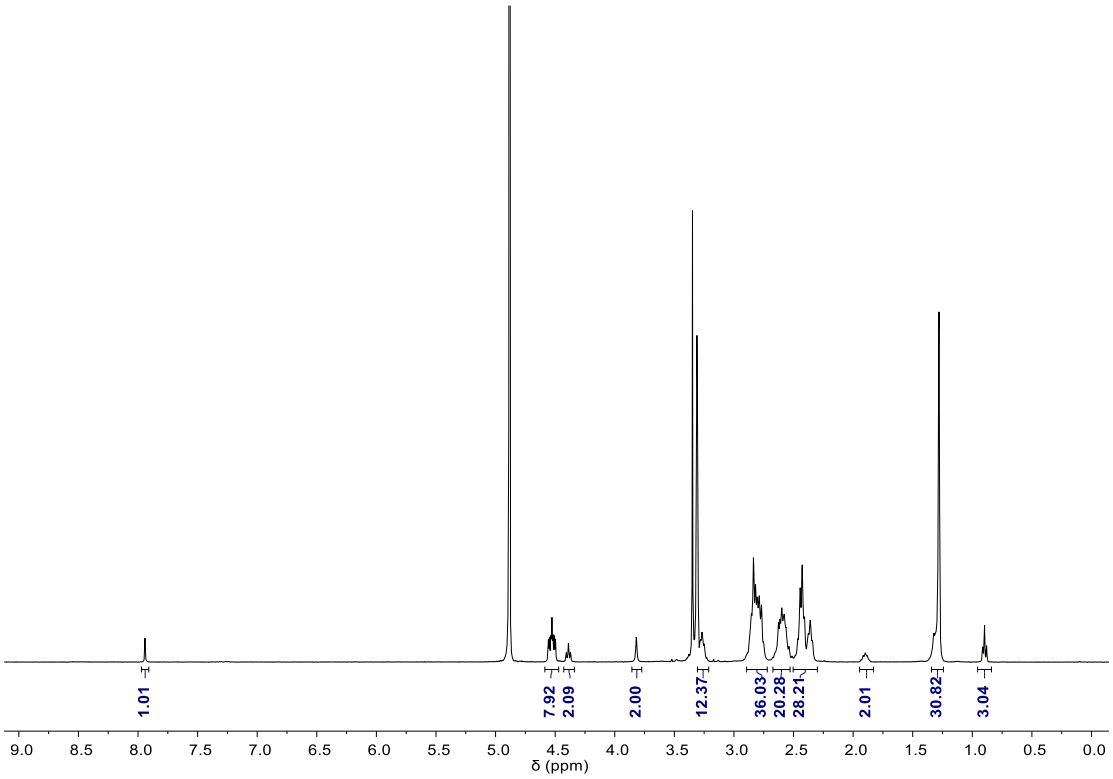

F. ^{13}C NMR of **1c** (151 MHz, $CD_3OD/CDCl_3$=1/1)

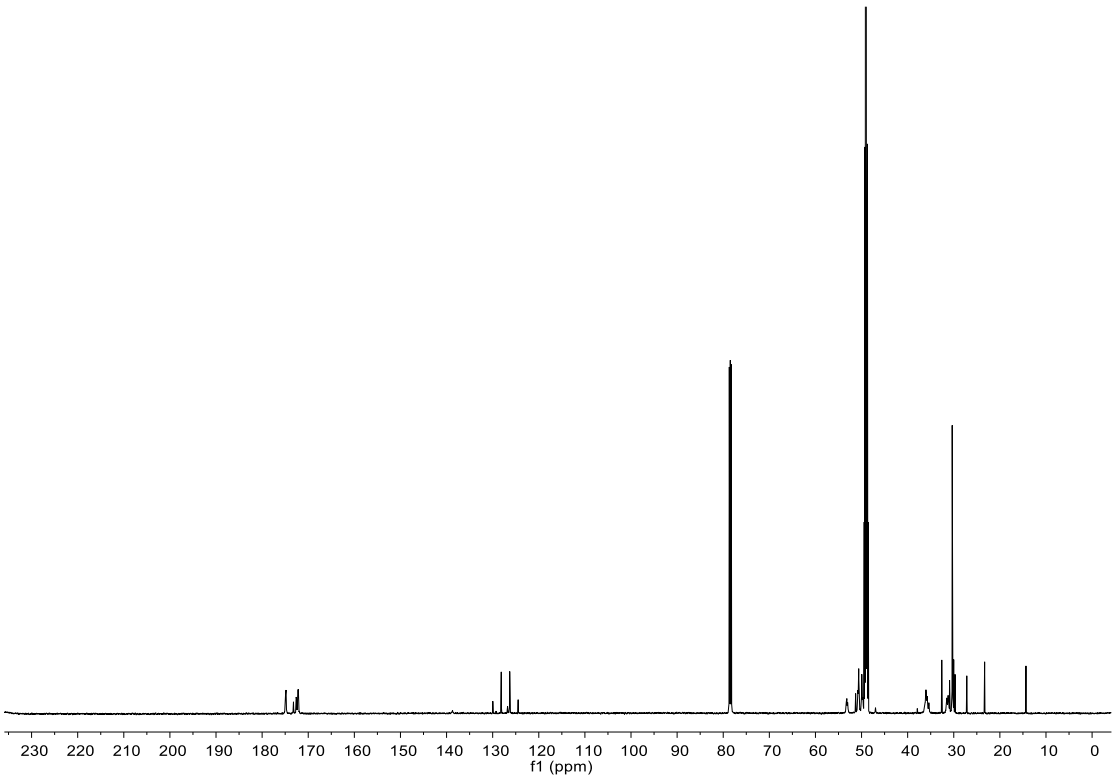

Fig. S3. (A) Hemolysis assay of **1c** using mouse red blood cells. (B) Hematoxylin and Eosin (H&E) staining of tissues from major organs of L-IPC xenograft mice after ^{19}F-MRI experiments (Scale bar: 100 μm). PBS or **1c**@ (0.20 mol **1c**/kg) was administrated intravenously into L-IPC xenograft mice.

A

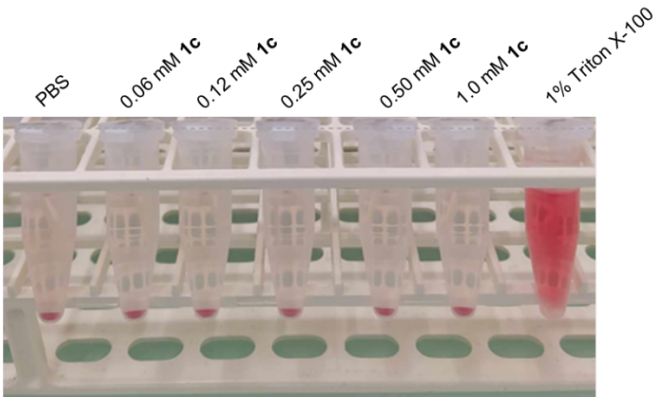

B

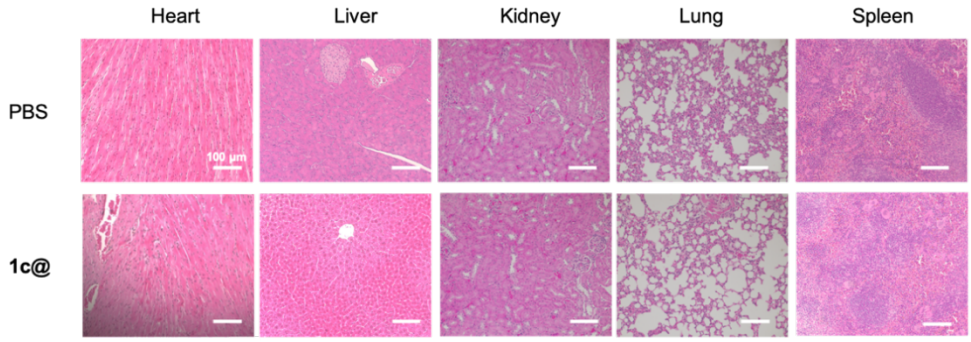

Fig. S4. Fluorescence emission (A) and absorbance (B) spectra of DiR in methanol.

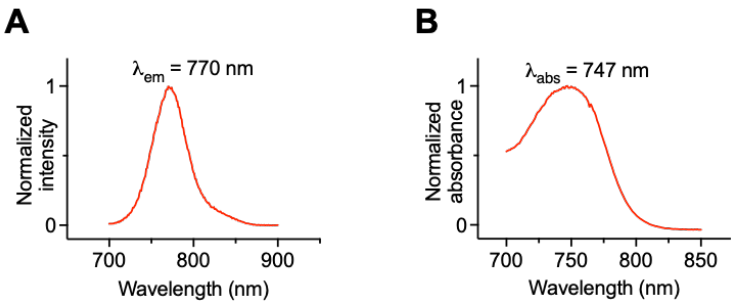

Fig. S5. ^{19}F NMR of PTX/**1c**@ (376 MHz, D_2O).

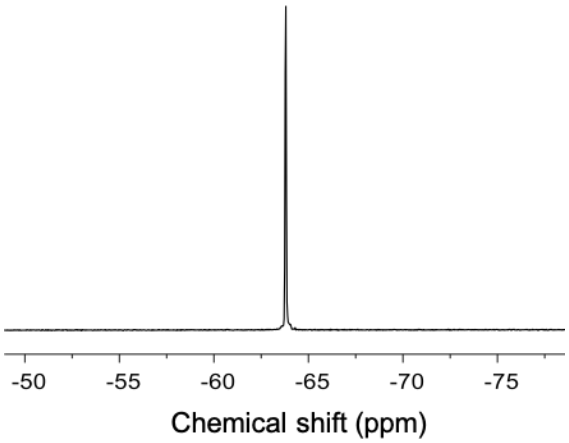

Fig. S6. Fluorescence emission (A) and absorbance (B) spectra of DiR/PTX/**1c**@ in water.

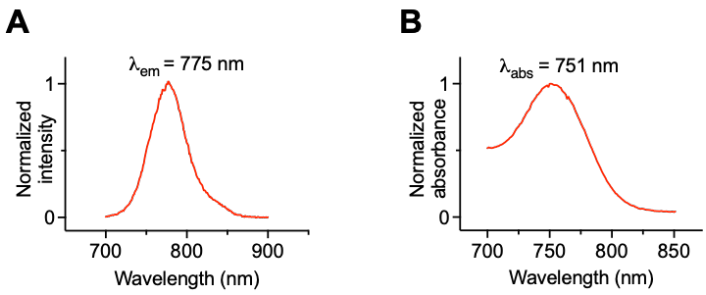

Fig. S7. Body weight of L-IPC xenograft mice treated with (A) PBS, PTX (7.5 mg·kg^{-1}), or PTX/DiR/**1c** @ (PTX 7.5 mg·kg^{-1}) (n = 3 per group) and (B) PBS, PTX (3.0 mg·kg^{-1}), **1c** @ or PTX/**1c** @ (PTX 3.0 mg·kg^{-1}) (n = 5 per group). The statistical significance was analyzed using one-way ANOVA with Dunnett's multiple comparison test (ns = no significance).

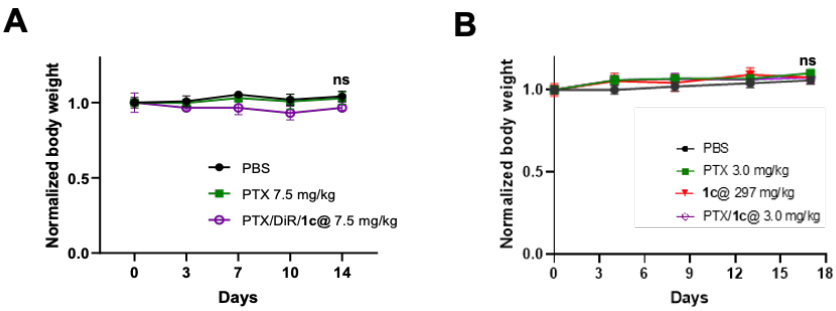

Fig. S8. Histological analysis of tissues from major organs of L-IPC xenograft mice after ^{19}F MRI experiments and treatment period using Hematoxylin and Eosin (H&E) staining (Scale bar: 100 μm). PBS, PTX, **1**@ or PTX/**1c**@ (3.5 mg PTX/kg) were administrated intravenously into L-IPC xenograft mice.

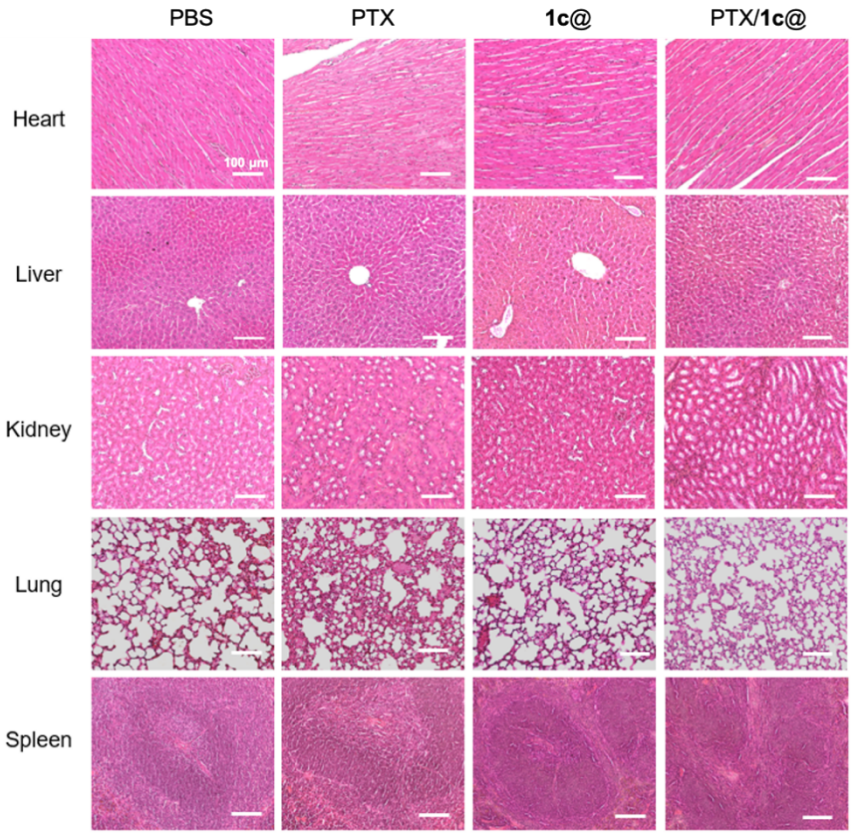

Synthesis and characterization of dendrimers

Fluorinated amino acid β-trifluoromethyl-alanine methyl ester hydrochloride (**F-Ala**) was purchased from Enamine (Kyiv, Ukraine). Other chemicals were purchased from Sigma Aldrich or Alfa Aesar. Methyl acrylate, ethylenediamine and dimethylformamide were dried according to the described methods and distilled before use. The other chemicals were used without further purification. Analytical thin layer chromatography (TLC) was performed using silica gel 60 F_{254} plates 0.2 mm thick with UV light (254 and 364 nm) as revelator. Chromatography was prepared on silica gel (Merck 200-300 mesh). Dialysis tubing was purchased from Sigma Aldrich (St. Quentin Fallavier, France) and Yuanye Bio-Technology Co., Ltd. (Shanghai, China). ^{1}H, ^{13}C and ^{19}F NMR spectra were recorded on Bruker Avance III 400 (400 MHz, ^{1}H; 101 MHz, ^{13}C; 376 MHz, ^{19}F), JEOL ECS 400 (400 MHz, ^{1}H; 101 MHz, ^{13}C; 376 MHz, ^{19}F) and Bruker Avance III 500 (500 MHz, ^{1}H; 125 MHz, ^{13}C; 471 MHz, ^{19}F) spectrometers. Chemical shifts (δ) are expressed in parts per million (ppm). MRI experiments were carried out on a BioSpec 70/16 US (Bruker BioSpin, Ettlingen, Germany) preclinical imaging system. The HRMS analysis was carried out with a SYNAPT G2 HDMS (Waters) mass spectrometer equipped with an electrospray ionization source operated in the positive-ion mode. High-resolution mass spectra (HRMS) were obtained with a time of flight (TOF) analyzer with orthogonal injection. Each accurate mass measurement was made in triplicate using an external calibration interface.

General synthesis route for dendrimer 1a-c

The ester-terminating dendrimers **2a-c** were synthesized according to the well-established protocol published by our group.[1] These ester-terminating dendrimers were hydrolyzed to offer the carboxylic acid-terminating dendrimers **3a-c**, followed by coupling with **F-Ala**. The obtained dendrimers **4a-c** were hydrolyzed with a base, and the final dendrimers **1a-c** were purified using dialysis.

Synthesis of the fluorinated amphiphilic dendrimer 1a

Synthesis of 3a

To a solution of **2a** (202 mg, 0.37 mmol) in MeOH (3.0 mL) in an ice bath, was slowly added $LiOH{\cdot}H_2O$ (65 mg, 1.6 mmol) in H_2O (3.0 mL). The solution was then stirred at 25ºC for 3 h, until the reaction was completed as indicated by NMR. The solvent was then removed under reduced pressure and the obtained crude extract dissolved in H_2O (5.0 mL). The pH was then adjusted to 3-4 using 1.0 M HCl solution, allowing precipitation of the dendrimer product. The aqueous phase was removed by filtration and the product was rinsed with H_2O (5.0 mL) then dried in a vacuum, giving the corresponding **3a** as a white solid (163 mg, 85%).

^{1}H NMR (400 MHz, DMSO-d_6): δ 8.03 (s, 1H), 4.29 (t, J = 7.0 Hz, 2H), 3.86 (s, 2H), 2.74 (t, J = 7.3 Hz, 4H), 2.48 (t, J = 7.1 Hz, 4H), 1.80-1.67 (m, 2H), 1.27 – 1.08 (m, 30H), 0.80 (t, J = 6.7 Hz, 3H); ^{13}C NMR (101 MHz, DMSO-d_6): δ 172.9, 140.9, 124.5, 49.3, 48.1, 46.9, 40.2, 39.9, 39.7, 39.5, 39.3, 39.1, 38.9, 31.4, 31.1, 29.7, 29.1, 29.0, 28.9, 28.8, 28.4, 25.8, 22.2, 14.0; HRMS: calcd. for $C_{27}H_{51}N_4O_4^+$ $[M+H]^+$ 495.3905, found 495.3906.

Synthesis of 4a

To a mixture of **3a** (51 mg, 0.12 mmol), **F-Ala** (51 mg, 0.25 mmol), HOBt (57 mg, 0.37 mmol) and EDCI (71 mg, 0.37 mmol) under Ar protection, was added DIPEA (25 μL, 0.25 mmol) in dry DMF (3.0 mL). The reaction was stirred at 25ºC for 2 days before removing the solvent under reduced pressure. The obtained residue was dissolved in CH_2Cl_2 (30 mL) and washed with saturated NH_4Cl solution (10.0 mL×2), saturated $NaHCO_3$ solution (10.0 mL×2) and brine (10.0 mL). The organic phase was dried over anhydrous Na_2SO_4, filtrated and concentrated. The crude product was purified using column chromatography on silica gel with CH_2Cl_2/MeOH = 35/1, giving the corresponding **4a** as a colorless sticky oil (62 mg, 63%). ^{1}H NMR (400 MHz, $CDCl_3$): δ 8.01 (dd, J = 7.4, 6.0 Hz, 2H), 7.53 (d, J = 3.0 Hz, 1H), 4.90-4.81 (m, 2H), 4.31 (t, J = 7.3 Hz, 2H), 3.85 (s, 2H), 3.78 (s, 6H), 2.86-2.66 (m, 8H), 2.57-2.46 (m, 4H), 1.95-1.83 (m, 2H), 1.34-1.21 (m, 30H), 0.86 (t, J = 6.9 Hz, 3H); ^{13}C NMR (101 MHz, $CDCl_3$): δ 172.2, 170.9, 142.9, 125.9 (q, J = 278.8 Hz), 122.9, 53.1, 50.5, 49.2, 47.3, 35.2 (q, J = 28.3 Hz), 33.3, 33.2, 32.1, 30.3, 29.8, 29.7, 29.7, 29.5, 29.1, 26.6, 22.8, 14.3; ^{19}F NMR (376 MHz, $CDCl_3$): δ -63.30. HRMS: calcd. for $C_{37}H_{63}F_6N_6O_6^+$ $[M+H]^+$ 801.4708, found 801.4708.

Synthesis of 1a

To a solution of **4a** (62 mg, 0.077 mmol) in MeOH (1.5 mL) in an ice bath, was slowly added $LiOH{\cdot}H_2O$ (13 mg, 0.31 mmol) in H_2O (1.5 mL). The solution was then stirred at 25ºC for 3 h, until the reaction was completed as indicated using NMR. The solvent was then removed under reduced pressure and the obtained crude extract dissolved in H_2O (5.0 mL), before adjusting the pH to 3-4 for extraction with CH_2Cl_2 (10.0 mL×3). The organic layer was collected and dried over anhydrous Na_2SO_4, before being filtered with the filtrate concentrated in a vacuum, giving the corresponding **1a** as sticky solid (44 mg, 75%).

^{1}H NMR (400 MHz, CD_3OD): δ 8.16 (s, 1H), 4.67 – 4.58 (m, 2H), 4.42 (t, J = 7.2 Hz, 2H), 4.32 (s, 2H), 3.29 – 3.16 (m, 4H), 2.95 – 2.57 (m, 8H), 1.96-1.86 (m, 2H), 1.40-1.23 (m, 30H), 0.90 (t, J = 6.8 Hz, 3H); ^{13}C NMR (101 MHz, CD_3OD/$CDCl_3$=1/1): δ 172.9, 170.5, 136.8, 126.2, 126.0 (q, J = 278.8 Hz), 53.4, 50.6, 46.7, 34.7 (q, J = 29.3 Hz), 31.8, 30.4, 30.3, 30.0, 29.6, 29.5, 29.4, 29.3, 29.22, 28.9, 26.4, 22.5, 13.9; ^{19}F NMR (376 MHz, CD_3OD): δ -65.65; HRMS: calcd. for $C_{35}H_{59}F_6N_6O_6^+$ $[M+H]^+$ 773.4400, found 773.4395.

Synthesis of the fluorinated amphiphilic dendrimer 1b

Synthesis of 3b

To a solution of **2b** (180 mg, 0.195 mmol) in MeOH (3.5 mL) in an ice bath, was slowly added $LiOH{\cdot}H_2O$ (65 mg, 1.6 mmol) in H_2O (3.5 mL). The solution was stirred at 25ºC for 3 h. When the reaction was complete, as revealed using NMR monitoring, MeOH was evaporated and the aqueous phase adjusted to pH 3-4 using 1.0 M HCl solution, before being subjected to dialysis (dialysis tubing, MWCO 500-1000, changing dialysis water every hour 6 times) and lyophilization. Cycles of dialysis and lyophilization were repeated 3 times to give **3b** as a white solid (135 mg, yield: 80%).

^{1}H NMR (400 MHz, CD_3OD): δ 8.29 (s, 1H), 4.48 (s, 2H), 4.44 (t, J = 7.2 Hz, 2H), 3.70-3.61 (m, 4H), 3.34-3.32 (m, 16H), 2.86 (t, J = 6.7 Hz, 4H), 2.66 (t, J = 6.2 Hz, 8H), 1.98-1.96 (m, 2H), 1.37-1.24 (m, 30H), 0.90(t, J = 8.0 Hz, 3H); ^{13}C NMR (101 MHz, CD_3OD): δ 176.8, 173.5, 138.1,

128.1, 53.0, 51.6, 50.0, 35.5, 33.1, 31.8, 31.3, 30.9, 30.8, 30.7, 30.6, 30.5, 30.2, 27.5, 23.7, 14.5; HRMS: calcd. for $C_{43}H_{80}N_8O_{10}^{2+}$ $[M+2H]^{2+}$ 434.2993, found 434.2988.

Synthesis of 4b

To a mixture of **3b** (104 mg, 0.12 mmol), F-Ala (129 mg, 0.62 mmol), HOBt (110 mg, 0.72 mmol), EDCI (138 mg, 0.72 mmol) and 4Å molecular sieves under Ar protection, was added DIPEA (63 μL, 0.62 mmol) in dry DMF (3.0 mL). The reaction mixture was stirred at 25ºC for 3 days. The solvent was then removed under reduced pressure and the obtained residue dissolved in CH_2Cl_2 (50 mL) and washed with saturated NH_4Cl solution (10.0 mL×2), saturated $NaHCO_3$ solution (10.0 mL×2) and brine (10.0 mL). The organic phase was then dried over anhydrous Na_2SO_4, filtrated and concentrated. The crude product was purified using column chromatography on silica gel with CH_2Cl_2/MeOH=20/1 (0.5% TEA), giving the corresponding **4b** as a pale brown oil (120 mg, 68%).

^{1}H NMR (500 MHz, $CD_3OD/CDCl_3$=1/1): δ 7.72 (s, 1H), 4.75-4.66 (m, 4H), 4.34 (t, J = 7.3 Hz, 2H), 3.78 (s, 2H), 3.74 (s, 12H), 3.25 (t, J = 6.6 Hz, 4H), 2.82 – 2.64 (m, 20H), 2.57 (t, J = 6.6 Hz, 4H), 2.43 – 2.37 (m, 12H), 1.93-1.84 (m, 2H), 1.32-1.21 (m, 30H), 0.86 (t, J = 6.9 Hz, 3H); ^{13}C NMR (126 MHz, $CD_3OD/CDCl_3$=1/1): δ 173.9, 171.3, 143.9, 126.4 (q, J = 277.2 Hz), 124.2, 53.2, 52.7, 51.0, 50.4, 49.6, 47.8, 47.1, 37.8, 35.4 (q, J = 29.0 Hz), 33.9, 33.6, 32.5, 30.8, 30.2, 30.2, 30.1, 30.0, 29.9, 29.6, 27.0, 23.2, 14.3; ^{19}F NMR (376 MHz, CD_3OD): δ -65.54; HRMS: calcd. for $C_{63}H_{105}F_{12}N_{12}O_{14}^{3+}$ $[M+3H]^{3+}$ 493.9222, found 493.9228.

Synthesis of 1b

To a solution of **4b** (60 mg, 0.041 mmol) in MeOH (2.0 mL) in an ice bath, was slowly added $LiOH{\cdot}H_2O$ (14 mg, 0.32 mmol) in H_2O (2.0 mL). The solution was stirred at 25ºC for 3 h. When the reaction was complete, as revealed using NMR monitoring, MeOH was evaporated and the aqueous phase adjusted to pH 3-4 using 1.0 M HCl solution, before subjecting to dialysis (dialysis tubing, MWCO 500-1000, changing dialysis water every hour 6 times) and lyophilization. Cycles of dialysis and lyophilization were repeated 3 times to give **1b** as a white solid (45 mg, yield: 78%).

^{1}H NMR (400 MHz, CD_3OD): δ 8.17 (s, 1H), 4.54-4.45 (m, 4H), 4.40 (t, J = 7.1 Hz, 2H), 4.26 (s, 2H), 3.51-3.42 (m, 4H), 3.26-2.94 (m, 16H), 2.89-2.77 (m, 4H), 2.71-2.49 (m, 16H), 1.94-1.84 (m, 2H), 1.36-1.24 (m, 30H), 0.90 (t, J = 8.0 Hz, 3H); ^{13}C NMR (101 MHz, CD_3OD): δ 175.5, 175.3, 174.0, 172.6, 138.6, 127.9 (q, J = 277.8 Hz), 127.8, 53.8, 51.6, 51.4, 51.2, 50.4, 47.4, 36.3 (q, J = 28.3 Hz), 33.1, 31.3, 31.1, 30.8, 30.7, 30.6, 30.5, 30.2, 27.5, 23.7, 14.5; ^{19}F NMR (376 MHz, CD_3OD): δ -65.51; HRMS: calcd. for $C_{59}H_{96}N_{12}O_{14}F_{12}^{2+}$ $[M+2H]^{2+}$ 712.3483, found 712.3492.

Synthesis of the fluorinated amphiphilic dendrimer 1c

Synthesis of 3c

To a solution of **2c** (300 mg, 0.17 mmol) in MeOH (5.0 mL) in an ice bath, was slowly added $LiOH{\cdot}H_2O$ (117 mg, 2.8 mmol) in H_2O (5.0 mL). The solution was then stirred at 25ºC for 3 h. When the reaction was complete, as indicated using NMR monitoring, MeOH was evaporated and the aqueous phase adjusted to pH 4.0 using 1.0 M HCl solution, then subjected to dialysis (dialysis tubing, MWCO 1000, changing dialysis water every hour for 6 times) and lyophilization. Repeating the operation cycles of dialysis and lyophilization for 3 times, the product was lyophilized to yield

the corresponding **3c** as a white solid (231 mg, yield: 83%).

^{1}H NMR (400 MHz, CD_3OD): δ 8.07 (s, 1H), 4.41 (t, *J* = 7.1 Hz, 2H), 4.13 (s, 2H), 3.70-3.60 (m, 12H), 3.49-3.24 (m, 36H), 3.01 (t, *J* = 6.8 Hz, 4H), 2.81 (t, *J* = 6.6 Hz, 8H), 2.68-2.59 (m, 20H), 1.95-1.87 (m, 2H), 1.36-1.24 (m, 30H), 0.90 (t, *J* = 6.7 Hz, 3H); ^{13}C NMR (101 MHz, CD_3OD): *δ* 177.2, 173.9, 173.3, 140.9, 126.8, 53.8, 53.0, 51.8, 51.4, 50.6, 50.1, 47.6, 35.6, 33.1, 32.5, 31.5, 31.3, 31.1, 30.8, 30.8, 30.7, 30.6, 30.5, 30.2, 27.6, 23.7, 14.5; HRMS: calcd. For $C_{75}H_{137}N_{16}O_{22}^{3+}$ $[M+3H]^{3+}$ 538.0026, found 538.0031

Synthesis of 4c

To a mixture of **3c** (160 mg, 0.087 mmol), F-Ala (248 mg, 1.0 mmol), HOBt (243 mg, 1.6 mmol), EDCI (305 mg, 1.6 mmol) and 4Å molecular sieves under Ar protection, was added DIPEA (106 μL, 1.0 mmol) in dry DMF (5.0 mL). The reaction was stirred at 25ºC for 3 days. The solution was then diluted with ethyl acetate (50 mL) and washed with saturated NH_4Cl solution (5.0 mL×3), saturated $NaHCO_3$ solution (10.0 mL×2) and brine (10.0 mL). The organic phase was dried over anhydrous Na_2SO_4, filtrated and concentrated. The crude product was purified using column chromatography on silica gel with CH_2Cl_2/MeOH=20/1 to 10/1 (0.5% TEA), giving the corresponding **4c** as a pale-yellow oil (151 mg, 61%).

^{1}H NMR (400 MHz, $CD_3OD/CDCl_3$=1/1): δ 7.78 (s, 1H), 4.75-4.68 (m, 8H), 4.34 (t, *J* = 7.2 Hz, 2H), 3.80 (s, 2H), 3.74 (s, 24H), 3.29-3.19 (m, 12H), 2.86 – 2.61 (m, 44H), 2.61-2.50 (m, 12H), 2.48-2.28 (m, 28H), 1.94-1.82 (m, 2H), 1.36-1.20 (m, 32H), 0.85 (t, *J* = 6.7 Hz, 3H); ^{13}C NMR (101 MHz, $CD_3OD/CDCl_3$=1/1): *δ* 174.0, 173.9, 171.3, 144.0, 126.5 (q, *J* = 277.8 Hz), 124.3, 53.2, 52.8, 51.0, 50.5, 50.3, 49.7, 47.8, 38.0, 37.9, 35.3 (q, *J* = 24.2 Hz), 34.0, 33.6, 32.5, 30.9, 30.3, 30.2, 30.0, 29.9, 29.6, 27.1, 23.2, 14.3; ^{19}F NMR (376 MHz, $CD_3OD/CDCl_3$=1/1): *δ* -64.65; HRMS: calcd. for $C_{115}H_{186}F_{24}N_{24}O_{30}^{4+}$ $[M+4H]^{4+}$ 710.0848, found 710.0847

Synthesis of 1c

To a solution of **4c** (80 mg, 0.028 mmol) in MeOH (4.0 mL) in an ice bath, was slowly added NaOH (10 mg, 0.25 mmol) in H_2O (1.0 mL). The solution was stirred at 25ºC for 3 h. When the reaction was complete, as indicated by NMR monitoring, MeOH was evaporated and the aqueous phase then adjusted to pH 3-4 using 1.0 M HCl solution, before being subjected to dialysis (dialysis tubing, MWCO 2000, changing dialysis water every hour 6 times) and lyophilization. Cycles of dialysis and lyophilization were repeated 3 times to give **1c** as a white solid (63 mg, yield: 82%).

^{1}H NMR (400 MHz, CD_3OD): *δ* 7.94 (s, 1H), 4.58-4.47 (m, 8H), 4.39 (t, *J* = 7.1 Hz, 2H), 3.82 (s, 2H), 3.31 – 3.21 (m, 12H), 2.89-2.72 (m, 36H), 2.67-2.53 (m, 20H), 2.50-2.30 (m, 28H), 1.95-1.83 (m, 2H), 1.34-1.24 (m, 30H), 0.90 (t, *J* = 6.6 Hz, 3H); ^{13}C NMR (151 MHz, $CD_3OD/CDCl_3$=1/1) δ 174.9, 174.8, 173.2, 172.6, 172.3, 172.2, 138.7, 127.2 (q, *J* = 277.8 Hz), 126.3, 53.3, 53.2, 53.0, 51.3, 50.8, 50.6, 50.0, 49.9, 49.7, 47.0, 37.8, 35.9 (q, *J* = 28.2 Hz), 35.4, 32.6, 31.5, 31.2, 31.1, 30.9, 30.3, 30.2, 30.1, 30.0, 29.7, 27.2, 23.3, 14.3; ^{19}F NMR (376 MHz, CD_3OD): δ -65.37; HRMS: calcd. for $C_{107}H_{169}F_{24}N_{24}O_{30}^{3+}$ $[M+3H]^{3+}$ 909.0689, found 909.0689

Critical micelle concentration (CMC)

CMC was determined using fluorescence spectrophotometry with Nile Red as the fluorescence probe. Dendrimer stock solution was prepared in water and aliquots were diluted with water to get the desired concentrations (0.10 μM to 500 μM) in 1.0 mL solution. 1.0 μL of Nile Red was added from its 2.5 mM stock solution prepared in ethanol and solutions were vortexed for 10 min and kept for 2 h at room temperature to promote the micelle formation prior to fluorescence measurement. Fluorescence spectra were recorded at the emission wavelength of 635 nm on a CARY Eclipse fluorescence spectrophotometer at room temperature. The excitation wavelength was 550 nm. The CMC value was determined by plotting normalized fluorescence intensity (dividing each fluorescence intensity by the maximal intensity) against the dendrimer concentrations.

Dynamic light scattering (DLS)

Dynamic light scattering (DLS) measurements were performed to determine the hydrodynamic diameter of the nanoparticles formed with amphiphilic dendrimers. The dendrimers were first dispersed in milliQ water at a concentration of 1.0 mM, and sonicated 30 seconds at 60 Hz (Ultrasonic Cleaner Branson B-200). Then size and zeta potential were measured using a Malvern Zetasizer Nano ZS equipped with a standard 633 nm laser at 25 °C. The experiments were carried out in triplicates.

Transmission Electron Microscopy (TEM)

Transmission electron microscopy (TEM) was performed using an JEOL-JEM-2100F analytical electron microscope (Tokyo, Japan) to characterize the size and morphology of the nanoparticles at an accelerating voltage of 200 kV. The nanoparticle solutions were prepared in milliQ water at a concentration of 1.0 mg/mL, vortexed for 15 seconds, then diluted to 10 μg/mL, followed by depositing an aliquot (4.0 μL) onto a carbon-coated copper grid during 15 minutes at 25°C. The excess of solution was removed by filter paper. The grid was then stained with 3.0 μL uranyl acetate (2.0 % in aqueous solution) for 5 seconds, and the excess uranyl acetate was removed by filter paper before measurements.

Isothermal Titration Calorimetry Studies

Isothermal titration calorimetry (ITC) experiments were performed with a MicroCal PEAQ-ITC calorimeter (Malvern, UK) at 298 K. The cell volume was 208 μL. The micellization experiments were conducted by step-by-step injections of a constant volume of concentrated **1c** solution into the calorimetric cell containing ultra-pure water. Specifically, a constant 2.0 μL portion of 2.0 mM **1c** solution was injected 18 times into the reaction cell at 120 s intervals. Upon filling cell and syringe, stirring was turned on and the system was allowed to thermally equilibrate for 30 minutes. The integrated ITC data were fitted to a sigmoidal function to yield the free enthalpy of micellization, ΔH_{mic}, as the difference between the final and the initial values of the integrated heat of the titration curve. The CMC is defined as the midpoint of the same curve. Finally, the aggregation number (N_{agg})

was estimated from the same data set using a protocol based on the two-state reaction model and the principle of mass conservation.[2-3]

Computational details

The dendrimer **1c** was parametrized according to a well-established procedure.[4-6] Partial charges were derived by the RESP procedure implemented in the RED server[7] while Gaff2 atom types[8] were assigned with the Antechamber of AmberTools. Forty-four (48) **1c** monomers were randomly placed in a cubic box filled with TIP3 waters[9] extending at least 20 Å from each solute molecule. The obtained systems were subjected to a combination of steepest descent/conjugate gradient minimization of the potential energy, followed by a gradually heating to 298 K by running 500 ps of atomistic molecular dynamics (AMD) simulations in the canonical (NVT) ensemble under periodic boundary conditions. The SHAKE algorithm[10] was applied to all covalent bonds involving hydrogen atoms. The Langevin thermostat[11] was adopted for temperature regulation and an integration time step of 2.0 fs was applied. The final heating step was followed by 50 ns of AMD equilibration in the isochoric/isothermal (NPT) ensemble. Pressure control was exerted by coupling the system to a Berendsen barostat. [12] The Particle Mesh Ewald (PME)[13] method was used to treat the system electrostatics with a direct space cut-off of 10 Å. Finally, the NPT AMD production run was performed for another 500 ns. In the production phase, pressure was controlled by the Monte Carlo barostat implemented in Amber 22.[14] All simulations were carried out using AMBER 22 on our own GPU/CPU hybrid cluster and the pre-exascale Tier-0 EuroHPC Leonardo supercomputer (CINECA, Bologna, Italy). Graphics and analysis were performed with the UCSF Chimera software[15] and the GraphPad Prism (v. 9) (GraphPad Software, www.graphpad.com).

Formulation methods for 1c@ nanoparticles

Dendrimer **1c** was used to encapsulate PTX and DiR via film dispersion method. PTX/**1c**@ were prepared by mixing dendrimer solution (2.0 mg/mL in MeOH, 1.0 mL) with different amounts of PTX (1.0 mg/mL in MeOH), then the solvent was removed by vacuum rotary evaporation to form a dry film. The dried film was then hydrated with 1.0 mL of H_2O. Nonencapsulated PTX was separated by filtration through a 0.45-μm polycarbonate membrane (Millipore Co.).

DiR/**1c**@ was prepared by mixing the dendrimer **1c** solution (6.0 mg/mL in MeOH, 1.0 mL) with the DiR solution (2.0 μg/mL in MeOH, 411 μL), while PTX/DiR/**1c**@ was prepared by mixing together the dendrimer **1c** solution (6.0 mg/mL in MeOH, 1.0 mL), DiR solution (2.0 μg/mL in MeOH, 411 μL) and the PTX solution (0.50 mg/mL in MeOH, 154 μL). Following the same procedure, the solvent was removed by vacuum rotary evaporation to form a dry film. The dried film was then hydrated with 1.0 mL of H_2O. Nonencapsulated PTX was separated by filtration through a 0.45-μm polycarbonate membrane (Millipore Co.).

MRI conditions and T_1/T_2 measurements

MRI experiments were carried out using a Pharmascan 70/16 US (Bruker BioSpin, Ettlingen, Germany) preclinical imaging system. The system was equipped with a 7 T horizontal magnet with an internal diameter of 16 cm. A gradient coil (BGA9S HP) with an internal diameter of 9 cm for a maximum gradient strength of 760 mT/m was used. The acquisitions were performed using a Bruker Radio Frequency (RF) surface coil $^{1}H/^{19}F$ with a diameter of 2 cm. The same RF coil was used for transmission and reception. Each ^{19}F concentration was imaged separately in a glass vial (NMR tube of 10 mm diameter the length of which had been reduced). First and second order shimming (uniformization of the magnetic field to minimize the fluorine line width) was performed before each experiment. The radiofrequency pulse power was adjusted in a 4 mm thick slice parallel to the coil. All *in vitro* MRI acquisitions were performed at 20°C. *In vivo* MRI was performed under ketamine/xylazine anesthesia (100 mg kg^{-1} / 10 mg kg^{-1}) and external heating of the mice to keep rectal temperature at 35 – 37 °C. The radiofrequency pulse power was adjusted in a 4 to 6 mm thick slice parallel to the coil to include the entire tumor depth. All *in vitro* and *in vivo* ^{19}F-acquisitions were performed with a field of view (FOV) of 64×64×16 mm^3 and a 32×32×8 matrix resulting in a voxel size of 2×2×2 mm^3.

T_1/T_2 measurements

Relaxometry was performed to estimate longitudinal (T_1) and transverse (T_2) relaxation time constants of the ^{19}F dendrimers. A 3D Multi Slice Multi Echo (MSME) sequence was used. The number of accumulations (NA) was 15 for high (10 mM) ^{19}F concentrations and at least 60 for low (2.5 mM) ^{19}F concentrations. The receiver gain (RG) was kept identical for all acquisitions that had to be compared to one another. Effective spectral bandwidth (BW) = 50 kHz.

T_1 relaxation times were obtained from differently T_1 weighted acquisitions with the following parameters: TE = 5 ms; TR = 4000, 3000, 1500, 1000, 750, 500, 200, 100 ms;

T_2 relaxation times were obtained from differently T_2 weighted acquisitions with the following parameters: TR = 4000 ms; Number of echoes = 120; TE = 5 ms with 5 ms echo spacing.

Signal analysis was performed using the simplex algorithm implemented in Image J (National Institute of Health, USA, version 1.53a). The longitudinal relaxation time constants were obtained by fitting a two-parameter exponential recovery model to the signal intensities. The transverse relaxation time constants were obtained by fitting a two-parameter exponential decay model to the signal intensities. Signal intensities where averaged over 9 voxels inside the sample.

^{19}F MRI of dendrimer solution

Using the same MRI equipment and image geometry, ^{19}F MRI was performed at 20°C using **1c**@, DiR/**1c**@ and PTX/**1c**@ at different concentrations (20.0 mM, 10.0 mM, 5.0 mM, 2.5 mM of ^{19}F) to estimate the detection limit in terms of fluorine concentration and to evaluate the signal linearity. ^{19}F MRI was acquired using a gradient echo sequence with the following parameters: TR = 4000 ms; TE = 1.25 ms; BW = 66 kHz; flip angle = 90°, and NA = 28 leading to a total acquisition

time of 29 min 52 s.

Cell culture

For *in vitro* and *in vivo* studies, the following cell lines were used: L-IPC (primary pancreatic adenocarcinoma) cells, HEK293 (human embryonic kidney 293 cells), L929 (mouse fibroblast cells) and CHO-K1 (Chinese hamster ovarian cells subclone). L-IPC cells, HEK 293 cells and L929 cells were maintained in DMEM (Gibco, Invitrogen) supplemented with 10% fetal bovine serum (FBS) (Biosera) while CHO-K1 cells were cultured in RPMI medium (Gibco, Invitrogen) with the addition of 10% FBS, at 37°C with 5% CO_2.

PrestoBlue assay

HEK 293, L929 and CHO-K1 cells were seeded at 4000 cells/well in 50 µL/well in 96 well plates and allowed to grow overnight. Cells were then treated with fluorinated dendrimers at various concentrations (0.01 - 1.0 mM) for 48 h in 100 µL/well final volume. After treatment, cell viability was assessed by adding 10 µL of the PrestoBlue™ Cell Viability Reagent (Invitrogen) and incubating for 3 hours, following the supplier's protocol. Cell viability was normalized to the rates of untreated cells. All samples were run in triplicate.

LDH assay

HEK 293, L929 and CHO-K1 cells were seeded at 4000 cells/well in 50µL/well in 96 well plates 24h prior to treatment. The cells were treated with fluorinated dendrimers at a concentration range of 0.01 – 1.0 mM and then incubated for 48 h at 37°C, 5% carbon dioxide and 95% humidity for 48h. Cell membrane damage was determined using CytoTox-ONE TM Homogeneous Membrane Integrity Assay (Promega). A fresh round-bottom 96-well plate was prepared, and each well received 50 µL of the LDH reaction mixture, following the manufacturer's protocol. Subsequently, 50 µL of blank, control, or treated cell samples were added to the respective wells. After incubating the plates at room temperature for 30 minutes, 50 µL of Stop solution provided by the manufacturer, was added. Fluorescence was measured at 490 nm using fluorescence spectroscopy. Positive and negative controls were performed with lysis buffer and medium, and set as 100% and 0% LDH release, respectively. Each assay was performed in triplicate. LDH% = [(the absorbance of sample – the absorbance of negative control) / (the absorbance of positive control – the absorbance of negative control)] ×100%.

Hemolysis assay

Blood (1.0 mL) was freshly collected from a 4-week-old female NMRI-Foxn1nu/nu mice (with 1.0% heparin sodium solution). Red blood cells (RBCs) were isolated by centrifuging at 5.0 × 10^3 rpm for 5.0 min. The obtained RBCs were washed several times with PBS buffer until no

color was visible in the supernatant, and then diluted in PBS to achieve a solution with a concentration of 2.0% (e.g. 20 μL of RBC suspension added to 0.98 mL PBS). This 2.0% RBC solution (0.50 mL) was added into 1.5 mL Eppendorf tubes, and 0.50 mL of **1c** at different concentrations were added to make the final concentrations of 0.06, 0.12, 0.25, 0.5, 1.0 mM **1c**. PBS and 1.0% TritonX-100 solutions (0.50 mL) were added to 2.0% RBC solution (0.50 mL), and used as the negative control and positive control, respectively. The samples were mixed gently, left at 37 °C for 1.0 h, then centrifuged at 1.0×10^4 rpm for 5.0 min. The supernatants (0.10 mL of) were transferred to a 96-well plate and the absorbance of hemoglobin at 540 nm was measured.[16]

The percentage of hemolysis was calculated as follows:

Hemolysis% = [(sample absorbance – negative control) / (positive control – negative control)] ×100%

Animals

For in vivo imaging studies, all procedures using animals were approved by the committee on ethics in animal research (Comité d'Ethique de Marseille n°14), authorized by the ministry of higher education, research and innovation (project authorization n°30203), and conducted according to the EU Directive 2010/63/EU. Female (4 weeks old) NMRI-Foxn1nu/nu mice were provided by Charles River Laboratories. Mice were kept within the Experimental Animal House of the Centre de Recherche en Cancérologie de Marseille, Pôle Luminy with a 12h light/12h dark cycle. Mice were housed in enriched cages placed in a temperature- and hygrometry-controlled room with daily monitoring, and were provided with water and commercial diet *ad libitum*. Five weeks after tumor cell inoculation, the mice were transferred to the Centre de Resonance Magnétique Biologique et Médicale where they could rest for two weeks before MRI experiments. Upon completion of MRI, the mice were transferred back to the Centre de Recherche en Cancérologie de Marseille for NIRF imaging.

For *in vivo* toxicity evaluation, all procedures were approved by the Institutional Animal Care and Use Committee of China Pharmaceutical University and performed in accordance with the guidelines and policies for *in vivo* toxicity evaluation experiments.[17-18] The approval number was "2023-07-007". Female ICR mice (6 weeks old) were purchased from Sino-British SIPPR/BK Lab Animal Ltd (Shanghai, China). The mice were maintained in China Pharmaceutical University Laboratory Animal Center during the experiment.

***In vivo* toxicity**

The mice were randomly divided into 3 groups (n = 3/group), and then administered 100 μL PBS (phosphate buffer saline, the negative control), LPS (lipopolysaccharide, 5.0 mg/kg, the positive control), and **1c** (286.5 mg/kg), respectively. PBS and **1c** were injected intravenously via the tail vein, while LPS was administrated intraperitoneally. Mice were sacrificed after 24 h. The serum specimens were collected to assess the inflammatory factors (IL-1β, IL-6, TNF-α, and IFN-γ) and biochemical parameters (ALT, AST, CREA, UREA, TG and TCHO). The excised organs

(hearts, livers, spleens, lungs, kidneys, and intestines) were fixed in 4% paraformaldehyde solution and embedded in paraffin, cut into 4 μm thick sections and stained with hematoxylin and eosin (H&E). The H&E-stained sections were then examined and photographed using a fluorescence microscope (Zeiss Axio Vert A1).

Mice ectopic xenograft models of pancreatic tumors

1.0×10^8 L-IPC (primary pancreatic adenocarcinoma) cells were resuspended in 0.25 mL PBS and 0.25 mL Matrigel Matrix (Corning, New York, USA). Then a volume of 50 μL of this mixture containing 1.0×10^7 L-IPC cells were injected subcutaneously into each lower flank of nude mice (5 weeks old). The tumors were allowed to grow for 6 weeks to reach a volume of 500 mm^3. The tumor volume was monitored using calipers in two dimensions and calculated using the following formula: V (mm^3) = L (mm) × W^2 (mm^2) × 0.5 (L being the longest tumor diameter and W the shortest).

***In vivo* ^{19}F MRI**

The anesthetized mice (with a mixture of ketamine (100 mg/kg) and xylazine (10 mg/kg)) were positioned in left decubitus with the tumor centered on the RF coil within the preclinical MRI scanner. After above-described adjustments and calibrations, for the group of mice injected with DiR/**1c**@, 2D ^{1}H- and ^{19}F-MRI was acquired using a fast gradient echo (FLASH, Fast Low Angle Shot) sequence as for the *in vitro* experiments on dendrimer solutions. For anatomical details the ^{1}H-MRI was acquired with 16 sagittal slices of 1 mm, 256 × 256 matrix (250 × 250 μm^2 spatial resolution), TR = 130 ms, TE = 2.5 ms, flip angle = 30°, BW = 66 kHz, total acquisition time 17 s. The lower resolution (2 × 2 mm^2) ^{19}F-MRI was acquired in the same position with 8 sagittal slices of 2 mm, 32 × 32 matrix, TR = 4 s, TE = 1.25 ms, flip angle = 90°, BW = 66 kHz, NA = 28, and a total acquisition time of 29 min 52 s.

3D acquisitions were acquired for the group treated with PTX/DiR/**1c**@: ^{1}H-MRI was acquired using a 3D FLASH sequence, matrix 256 × 256 × 16 (250 × 250 × 1000 μm^3 spatial resolution), TR = 50 ms, TE = 1.6 ms, flip angle = 80°, BW = 90 kHz, and with a total acquisition time of 2 min 45 s. ^{19}F-MRI was acquired in the same position but with reduced resolution (2 × 2 × 2 mm^3) using a fast spin echo sequence (acceleration factor 32), matrix 32 × 32 × 8, TR = 4 s, TE = 1.75 ms, flip angle = 90°, BW = 100 kHz, NA = 55, and total acquisition time of 29 min 20 s.

***In vivo* NIRF imaging**

The L-IPC tumor bearing mice were visualized simultaneously (n = 3) by using the imaging system Photon IMAGER (Biospace Lab) with excitation at 740 nm and emission at 790 nm using an exposure time of 1000 milliseconds. The system was equipped with an intensified charge-coupled device (ICCD) camera. During imaging, mice were anesthetized with isoflurane (1-2% at a flow

rate of 0.3 - 0.5 L/min for 3-5 minutes). A 740 nm pulsed laser diode was used to excite the DiR molecules. Emission wavelength at 770 nm was collected. NIRF images were processed with M3 Vision (Biospace Lab). PBS and the free fluorescent dye DiR were used as controls.

In vivo anticancer evaluation

When the tumor sizes reached ~150 mm^3, PBS, free PTX (7.5 mg/kg) or PTX/DiR/**1c**@ at a PTX equivalent dose of 7.5 mg/kg was intravenously administered into the mice twice per week for two weeks. The PBS and PTX groups of mice were used as controls for the PTX/DiR/**1c**@ group (n=3).

In another *in vivo* study, when the tumor sizes reached ~150 mm^3, PBS, free PTX (3.0 mg/kg), **1c**@ or PTX/**1c**@ at a PTX equivalent dose of 3.0 mg/kg was intravenously administered into the mice twice per week for two weeks. The PBS group and **1c**@ group were used as controls for the PTX and PTX/**1c**@ groups (n=5 per group).

Mouse body weight was recorded to evaluate the toxicity. Tumor volume was measured twice per week using a caliper as described above. At the end of the experiments, tumors and major organs were excised and subjected to histochemical analysis.

Hematoxylin and eosin staining

Excised organs were washed with PBS and fixed in formalin for 48 hours. After fixation, the samples were dehydrated first in a graded ethanol series and then in xylene. Subsequently, samples were embedded in paraffin, and the embedded tissues were cut into 4 μm slices using a Leica microtome and then dried. The tissue sections were stained with hematoxylin and eosin (Sigma), following the manufacturer's instructions. Finally, micrographs were taken using a ZEISS Axio Imager Z2 microscope.

Immunohistochemistry

The 4-micrometer paraffin sections of the tumor underwent incubation at 65°C for 1.5 hours and were subsequently rehydrated. To reveal antigenic sites, the slides were incubated in Dako's Buffer (Citrate) TRS pH 6 at 96°C for 20 minutes and then at room temperature for an additional 30 minutes. Following the blocking of endogenous peroxidases with 3% H_2O_2 for 10 minutes, the slides underwent three rinses with PBS. Next, the slides were incubated with Abcam's Monoclonal Rabbit Anti-Human Ki-67 antibody (1:100) or Rabbit Cleaved Caspase-3 (Asp175) antibody (Cell Signaling Technology, 1/100) for 60 minutes at room temperature. After three washes in PBS, the slides were treated with Abcam's Goat anti Rabbit Ig biotinylated secondary antibody (1:400) for 30 minutes at room temperature. Subsequently, Streptavidin-HRP (Agilent; 1:500) was added for 30 minutes at room temperature to facilitate staining. The staining was visualized by adding DAKO's diaminobenzidine for 10 minutes at room temperature. After rinsing with distilled water,

the slides were incubated with Mayer's Hematoxylin for 30 seconds and then blued with a 0.1% sodium bicarbonate solution for 3 minutes. Finally, the slides were dehydrated, cleared, and mounted with coverslips using permanent mounting liquid. Images of the sections were captured using the ZEISS Axio Imager Z2 microscope.

TUNEL assay

Serial 4 µm sections were cut from the paraffin-embedded tumors. The analysis of apoptotic cells was conducted using the TUNEL apoptosis assay kit (Abcam) following the manufacturer's protocol. Subsequently, photomicrographs of the sections were captured using the ZEISS Axio Imager Z2 microscope.

Statistics:

Results were expressed as mean ± standard deviation. For in vivo studies, two groups and one time-point were compared with a standard two-tailed t-test. More than two groups and one time-point were compared using a one-way analysis of variance (ANOVA), and more than two groups and multiple time points were compared using two-way ANOVA. All analyzes were performed with Prism® software (GraphPad Software). $P < 0.05$ indicated statistical significance.

References:

1. Yu, T.; Liu, X.; Bolcato-Bellemin, A.-L.; Wang, Y.; Liu, C.; Erbacher, P.; Qu, F.; Rocchi, P.; Behr, J.-P.; Peng, L., An Amphiphilic Dendrimer for Effective Delivery of Small Interfering RNA and Gene Silencing In Vitro and In Vivo. *Angew. Chem. Int. Ed.* **2012,** *51* (34), 8478-8484.

2. Olesen, N. E.; Westh, P.; Holm, R., Determination of thermodynamic potentials and the aggregation number for micelles with the mass-action model by isothermal titration calorimetry: A case study on bile salts. *J. Colloid Interface Sci.* **2015,** *453*, 79-89.

3. Laurini, E.; Aulic, S.; Skoko, N.; Marson, D.; Fermeglia, M.; Pricl, S., ITC for Characterization of Self-Assembly Process of Cationic Dendrons for siRNA Delivery. In *Design and Delivery of SiRNA Therapeutics*, Ditzel, H. J.; Tuttolomondo, M.; Kauppinen, S., Eds. Springer US: New York, NY, 2021; pp 245-266.

4. Garrigue, P.; Tang, J.; Ding, L.; Bouhlel, A.; Tintaru, A.; Laurini, E.; Huang, Y.; Lyu, Z.; Zhang, M.; Fernandez, S.; Balasse, L.; Lan, W.; Mas, E.; Marson, D.; Weng, Y.; Liu, X.; Giorgio, S.; Iovanna, J.; Pricl, S.; Guillet, B.; Peng, L., Self-assembling supramolecular dendrimer nanosystem for PET imaging of tumors. *Proceedings of the National Academy of Sciences* **2018,** *115* (45), 11454-11459.

5. Ding, L.; Lyu, Z.; Tintaru, A.; Laurini, E.; Marson, D.; Louis, B.; Bouhlel, A.; Balasse, L.; Fernandez, S.; Garrigue, P.; Mas, E.; Giorgio, S.; Pricl, S.; Guillet, B.; Peng, L., A self-assembling amphiphilic dendrimer nanotracer for SPECT imaging. *Chem. Commun.* **2020,** *56* (2), 301-304.

6. Ding, L.; Lyu, Z.; Louis, B.; Tintaru, A.; Laurini, E.; Marson, D.; Zhang, M.; Shao, W.; Jiang,

Y.; Bouhlel, A.; Balasse, L.; Garrigue, P.; Mas, E.; Giorgio, S.; Iovanna, J.; Huang, Y.; Pricl, S.; Guillet, B.; Peng, L., Bioimaging: Surface Charge of Supramolecular Nanosystems for In Vivo Biodistribution: A MicroSPECT/CT Imaging Study (Small 37/2020). *Small* **2020,** *16* (37), 2070203.
7. Vanquelef, E.; Simon, S.; Marquant, G.; Garcia, E.; Klimerak, G.; Delepine, J. C.; Cieplak, P.; Dupradeau, F. Y., R.E.D. Server: a web service for deriving RESP and ESP charges and building force field libraries for new molecules and molecular fragments. *Nucleic Acids Res.* **2011,** *39* (Web Server issue), W511-7.
8. Träg, J.; Zahn, D., Improved GAFF2 parameters for fluorinated alkanes and mixed hydro- and fluorocarbons. *J. Mol. Model.* **2019,** *25* (2), 39.
9. Jorgensen, W. L.; Chandrasekhar, J.; Madura, J. D.; Impey, R. W.; Klein, M. L., Comparison of simple potential functions for simulating liquid water. *The Journal of Chemical Physics* **1983,** *79* (2), 926-935.
10. Ryckaert, J.-P.; Ciccotti, G.; Berendsen, H. J. C., Numerical integration of the cartesian equations of motion of a system with constraints: molecular dynamics of n-alkanes. *Journal of Computational Physics* **1977,** *23* (3), 327-341.
11. Wu, X.; Brooks, B. R., Self-guided Langevin dynamics simulation method. *Chem. Phys. Lett.* **2003,** *381* (3), 512-518.
12. Berendsen, H. J. C.; Postma, J. P. M.; van Gunsteren, W. F.; DiNola, A.; Haak, J. R., Molecular dynamics with coupling to an external bath. *The Journal of Chemical Physics* **1984,** *81* (8), 3684-3690.
13. Darden, T.; York, D.; Pedersen, L., Particle mesh Ewald: An N · log(N) method for Ewald sums in large systems. *The Journal of Chemical Physics* **1993,** *98* (12), 10089-10092.
14. Case, D. A.; Aktulga, H. M.; Belfon, K.; Ben-Shalom, I. Y.; Berryman, J. T.; Brozell, S. R.; Cerutti, D. S.; III, T. E. C.; Cisneros, G. A.; Cruzeiro, V. W. D.; Darden, T. A.; Forouzesh, N.; Giambasu, G.; Giese, T.; Gilson, M. K.; Gohlke, H.; Goetz, A. W.; Harris, J.; Izadi, S.; Izmailov, S. A.; Kasavajhala, K.; Kaymak, M. C.; King, E.; Kovalenko, A.; Kurtzman, T.; Lee, T.; Li, P.; Lin, C.; Liu, J.; Luchko, T.; Luo, R.; Machado, M.; Man, V.; Manathunga, M.; Merz, K. M.; Miao, Y.; Mikhailovskii, O.; Monard, G.; Nguyen, H.; O'Hearn, K. A.; Onufriev, A.; Pan, F.; Pantano, S.; Qi, R.; Rahnamoun, A.; Roe, D. R.; Roitberg, A.; Sagui, C.; Schott-Verdugo, S.; Shajan, A.; Shen, J.; Simmerling, C. L.; Skrynnikov, N. R.; Smith, J.; Swails, J.; Walker, R. C.; Wang, J.; Wang, J.; Wei, H.; Wu, X.; Xiong, Y.; Xue, Y.; York, D. M.; Zhao, S.; Zhu, Q.; Kollman, P. A., *Amber 2023*. University of California, San Francisco: 2023.
15. Pettersen, E. F.; Goddard, T. D.; Huang, C. C.; Couch, G. S.; Greenblatt, D. M.; Meng, E. C.; Ferrin, T. E., UCSF Chimera--a visualization system for exploratory research and analysis. *J. Comput. Chem.* **2004,** *25* (13), 1605-12.
16. Dong, Y.; Yu, T.; Ding, L.; Laurini, E.; Huang, Y.; Zhang, M.; Weng, Y.; Lin, S.; Chen, P.; Marson, D.; Jiang, Y.; Giorgio, S.; Pricl, S.; Liu, X.; Rocchi, P.; Peng, L., A Dual Targeting Dendrimer-Mediated siRNA Delivery System for Effective Gene Silencing in Cancer Therapy. *J. Am. Chem. Soc.* **2018,** *140* (47), 16264-16274.
17. Yang, W.; Wang, L.; Mettenbrink, E. M.; DeAngelis, P. L.; Wilhelm, S., Nanoparticle Toxicology. *Annu. Rev. Pharmacol. Toxicol.* **2021,** *61*, 269-289.
18. Ding, L.; Lyu, Z.; Perles-Barbacaru, T.-A.; Huang, A. Y.-T.; Lian, B.; Jiang, Y.; Roussel, T.; Galanakou, C.; Giorgio, S.; Kao, C.-L.; Liu, X.; Iovanna, J.; Bernard, M.; Viola, A.; Peng, L.,

Modular Self-Assembling Dendrimer Nanosystems for Magnetic Resonance and Multimodality Imaging of Tumors. *Adv. Mater.* **2024,** *36* (7), 2308262.